


Ferromagnetic Resonance Modes in the Exchange-Dominated Limit in Cylinders of Finite Length

Jinho Lim^{1,*}, Anupam Garg¹, and J. B. Ketterson^{1,2}

¹*Department of Physics and Astronomy, Northwestern University, Evanston, Illinois 60208, USA*

²*Department of Electrical and Computer Engineering, Northwestern University, Evanston, Illinois 60208, USA*

 (Received 19 January 2021; revised 1 September 2021; accepted 22 September 2021; published 2 December 2021)

We analyze the magnetic mode structure of axially magnetized finite-length nanoscopic cylinders in a regime where the exchange interaction dominates, along with simulations of the mode frequencies of the ferrimagnet yttrium iron garnet. For the bulk modes, we find that the frequencies can be represented by an expression given by Herring and Kittel by using wavevector components obtained by fitting the mode patterns emerging from these simulations. In addition to the axial, radial, and azimuthal modes that are present in an infinite cylinder, we find localized “cap modes” that are “trapped” at the top and bottom cylinder faces by the inhomogeneous dipole field emerging from the ends. Semiquantitative explanations are given for some of the modes, in terms of a one-dimensional Schrodinger equation, which is valid in the exchange-dominant case. The assignment of the azimuthal-mode number is carefully discussed, and the frequency splitting of a few pairs of nearly degenerate modes is determined through the beat pattern emerging from them.

DOI: [10.1103/PhysRevApplied.16.064007](https://doi.org/10.1103/PhysRevApplied.16.064007)

I. INTRODUCTION

With recent advances in submicron patterning techniques, dynamic magnetic studies of arrays of objects (so as to have large signals), for which the largest dimension is a few hundred nanometers or less, are attracting increasing attention. With advanced techniques, it is even possible to probe the dynamic properties of individual submicron particles [1–3]. Measurements on such samples can even be performed in the absence of an external field, i.e., solely in the presence of the internal demagnetization field (for shapes where such a field exists), provided the sample is small enough to be in a single-domain state [4]. Modes with an odd number of maxima and minima can be excited directly with a uniform microwave field; coupling to modes with higher wave numbers will be more challenging [5].

Here, we report on an exhaustive numerical study, using the OOMMF micromagnetic simulation code [6], of the resonance modes of yttrium iron garnet (YIG) cylinders, primarily of diameter $d = 75$ nm and height $h = 300$ nm, although some aspects are studied for other values of h (7.5–1200 nm). Our methodology shares many features with the work of McMichael and Stiles [7] on two-dimensional elliptical disks and three-dimensional thin cylindrical disks. Our three-dimensional geometry displays a much richer mode structure, however, requiring

a more detailed theoretical framework. In addition, we also develop techniques to resolve modes that are nearly degenerate in frequency.

Here, we are primarily concerned with *size-quantization effects* arising from finite sample dimensions. In particular, we will examine the mode spectrum in samples having a cylindrical shape with radius a (and corresponding diameter $d = 2a$) and height h , both analytically and numerically. Due to the ease of preparation of some materials as wires, such samples are widely studied experimentally, e.g., in Permalloy [8] and in Ni [9,10]. Cylinders of finite length with h/d ratios of order unity and larger can be readily patterned using optical and e -beam lithography by creating hole arrays in a resist followed by deposition and lift-off [11].

A. Theoretical background

Free spins in a magnetic field, H , precess at the Larmor frequency, $\omega = \gamma H$, where $\gamma = g|e|/2mc$ with g , e , and m being the electron g factor, charge, and mass, respectively. As noted, in materials with internal magnetization, additional fields are present that can alter the precession frequency. To describe this and related effects, Landau and Lifshitz [12] (LL) introduced the following equation of motion:

$$\frac{d\mathbf{M}}{dt} = -\gamma \mathbf{M} \times \mathbf{H} - \frac{\alpha\gamma}{M_0} \mathbf{M} \times (\mathbf{M} \times \mathbf{H}), \quad (1)$$

*jinholim15.2014@u.northwestern.edu

where \mathbf{H} is the total field at a given position within the sample arising from the external field plus that produced by the magnetization itself and an effective field arising from quantum-mechanical exchange; it can also include crystalline anisotropy, but this is suppressed in what follows. The second term on the right-hand side of Eq. (1) is incorporated to phenomenologically account for damping, which will largely be neglected in what follows. In addition to satisfying Eq. (1), \mathbf{M} and \mathbf{H} must satisfy appropriate boundary conditions at the surface of the body.

For ellipsoidal samples (including degenerate forms thereof), and in the presence of a homogeneous external field \mathbf{H} , the magnetization \mathbf{M} is nominally homogeneous, as is the resulting demagnetization field; one can then observe sharp absorption lines in ferromagnetic resonance (FMR) experiments (in the absence of strong damping), with all spins then seeing the same local field. The resonance frequency of this uniformly precessing mode in a spheroidal sample (where two of the principal axes of the ellipsoid are identical) with the external field, H_0 , along the axis of rotation is given by what is commonly called the Kittel formula [13]:

$$\omega = \gamma[H_0 + 4\pi(N_{\perp} - N_{\parallel})M_0], \quad (2)$$

where N_{\perp} and N_{\parallel} are coefficients accounting for the effect of demagnetization perpendicular and parallel to the rotation axes (with $2N_{\perp} + N_{\parallel} = 1$), respectively, and M_0 is the internal magnetization, which is taken as a constant; notably, γ may differ from the free-space value due to atomic and solid-state effects.

In addition to the uniformly precessing mode, there are nonuniform modes [14], which we can characterize

by some effective wavelength, λ . At shorter (nanometer-scale) wavelengths, the exchange interaction dominates, and the associated modes are termed exchange modes, as introduced by Bloch [15]. The importance of modes with longer wavelengths (in suitably large samples) was emphasized by Clogston *et al.* [16,17]. They arise from the solution of Eq. (1) together with $\nabla \cdot \mathbf{B} = 0$ and the Maxwell boundary conditions; they are commonly referred to as *magnetostatic modes*. Modes in the region where both exchange and magnetostatic effects compete are called dipole-exchange modes.

For the case of a sphere, some of the low-lying magnetostatic modes were examined by Mercerau and Feynman [18]. They were later studied in much greater detail for spheroidal samples by Walker [19].

For the case of an infinitely long cylinder ($N_{\perp} = 0.5; N_{\parallel} = 0$), with H_0 parallel to the rotational axis, which is relevant for the work presented here, the mode structure was studied by Joseph and Schlomann [20]. Here, we encounter families of purely azimuthal as well as radially quantized modes propagating up and down the cylinder axis, which approach $\omega = \gamma H_0$ at large k (in the absence of exchange). Recently, this problem was reexamined by Arias and Mills [21], who also considered the effects of exchange via perturbation theory.

At shorter wavelengths, the effects of exchange contribute. In this regime, the frequency of a mode with wavevector $k = 2\pi/\lambda$ for a spheroidal sample with external field H_0 aligned along the rotational axis can be described by the Herring-Kittel (HK) formula [22], which we discuss in Appendix A:

$$\omega = \gamma \sqrt{(H_0 - 4\pi N_{\parallel} M_0 + D_{\text{ex}} \mathbf{k}^2)(H_0 - 4\pi N_{\parallel} M_0 + D_{\text{ex}} \mathbf{k}^2 + 4\pi M_0 \sin^2 \theta)}, \quad (3)$$

where D_{ex} is a parameter measuring the strength of exchange (see below); $\mathbf{k}^2 = k_z^2 + k_{\perp}^2$, where k_z and k_{\perp} are the components of the wavevector parallel and perpendicular to the spheroid axis, respectively; and $\theta = \tan^{-1}(k_{\perp}/k_z)$ is the angle between the spin-wave propagation direction and the spheroid axes. Note that at $\mathbf{k} = 0$, the factor involving N_{\perp} that appears in Eq. (2) is *absent* from Eq. (3), since it is assumed that the transverse demagnetization field is “screened out” at short wavelengths. Indeed, ω is ill defined at precisely $\mathbf{k} = 0$, since θ is ambiguous. This shortcoming also signals the importance of the magnetostatic modes at intermediate \mathbf{k} values, i.e., as the sample size is reduced, there is a crossover between dipole-dominated and exchange-dominated modes. Modes with

\mathbf{k} values straddling these regimes are the dipole-exchange modes mentioned above. At short wavelengths, which will be the case in sufficiently small samples, Eq. (3) should provide a representation of the mode structure in rotationally symmetric samples, provided suitable quantized values of k_{\perp} and k_z are available; we will utilize Eq. (3) to represent some of our finite-size sample simulations in what follows.

More generally, and in the absence of exchange effects, magnetostatic effects will dominate the mode frequencies, which, for a spheroid, will lie in the range

$$\gamma(H_0 - 4\pi N_{\parallel} M_0 + 2\pi M_0) \geq \omega \geq \gamma(H_0 - 4\pi N_{\parallel} M_0). \quad (4)$$

Note that the number of modes in this interval is bounded only by the number of spins, i.e., the mode density is very high, making the resolution of individual modes extremely difficult at shorter wavelengths (where they pile up). When exchange is present, the mode frequencies are spread over a much wider interval.

In an inhomogeneous external field, or for samples with an arbitrary shape, one might initially expect to observe a broadened line (as happens in most nuclear-magnetic-resonance experiments). However, in the presence of exchange, this is not the case and well-defined modes emerge, as will be discussed further below.

B. Plan of the paper

We develop the theoretical framework for our problem in Sec. II, beginning with a discussion of cylindrical symmetry and the resulting angular-momentum quantum number (or azimuthal-mode number) in Sec. II A. In the magnetostatic limit, it is convenient to take this as the total angular momentum, m , as done by Walker, and by Joseph and Schlomann. In the exchange-dominated limit, it becomes more important to understand the separation of the angular momentum into its orbital and spin parts. The major component of a mode has spin $m_s = 1$ and orbital angular momentum $m_l = p$, and there is a small admixture of $m_s = -1$ and $m_l = p + 2$. Accordingly, we find it better to label the modes by the orbital angular momentum, p , of the major component. This is especially so when examining the computer-generated mode patterns, since the orbital behavior of any component of \mathbf{M} is immediately apparent.

That the two components of a mode are so unequal goes hand in hand with the fact that modes with $m_l = p$ and $-p$ are nearly degenerate, as we discuss in Sec. II B. A clear understanding of this issue is important, as this near degeneracy can lead to some confusion when looking at the mode patterns. In one case, we resolve this degeneracy (see Sec. III D) by exciting and examining the beat pattern between the $\pm p$ modes.

In Sec. II C, we show that exchange-dominated modes in long cylinders are approximately described via a Schrodinger-like equation for a particle in a cylindrical box with a modified boundary condition, such that the axial and radial dependence of the mode function factorizes, and the resulting quantization gives rise to axial and radial mode numbers. In an infinite cylinder, this separation is exact, which is exploited to good effect in the analyses of Joseph and Schlomann and of Arias and Mills. In a finite cylinder, the separation is approximate, since the demagnetizing field is nonuniform and flares away from the axis near the perimeter of caps at $z = 0$ and $z = h$. We give a semi-quantitative argument in Sec. II D that the Schrodinger equation possesses bound-state solutions near these caps, corresponding to “cap modes,” which we see very clearly

in our simulations. For any p , there are two such modes (one for each cap), the frequencies of which lie below those of the bulk modes with the same p . This means that the uniform FMR or Kittel mode, which is the lowest bulk mode with $p = 0$, is not the lowest-frequency mode of the body. For this case, we present numerical results for the solution of the Schrodinger equation in Sec. II E and find good agreement with the simulations.

The cap modes are an unexpected feature of our study, as they do not exist in an infinite cylinder or a finite-sized ellipsoid of revolution. Similar “end modes” were found by McMichael and Stiles [7], who did not, however, investigate their origin. We expect that such localized modes will exist near the surfaces of other sample shapes as well as whenever the demagnetizing field departs significantly from uniformity.

Our simulation approach is described in Sec. III. It is based on the OOMMF code developed at the National Institute of Standards and Technology. After finding the static equilibrium magnetization, $\mathbf{M}_{eq}(\mathbf{r})$ (Sec. III A), we excite the system by applying pulses that are localized in space, time, or both [23]. The spatial center and the width and frequency bandwidth are varied, depending on which mode(s) we wish to excite. The resulting time development of $\mathbf{M}(\mathbf{r}, t)$ is Fourier transformed, and the point-wise power spectrum is added over all the cells. The resulting sum displays peaks at many mode frequencies, and by honing in on individual peaks, we can identify the magnetization patterns for each mode, as explained in Sec. III C

Once a particular mode pattern is obtained in a simulation, it can be used as is or altered in some way, say by combining it with some other mode, to study the subsequent development in time. This is a potentially promising way to study mode-mode coupling or large-amplitude responses, which we hope to pursue in the future. As an application of this idea, and as noted above, $\pm p$ modes are sometimes nearly degenerate, as are the even and odd superpositions of the cap modes. In Sec. III D, we show that, by starting the simulation in a suitable real-space pattern, we can find a beat pattern in the time development of the magnetization from which we can obtain the frequency splitting of the modes. We perform this exercise for only a few cases, as it is computationally intensive, and the physical principles are the same for the other cases.

In Sec. IV, we tabulate the frequencies of all the modes we find (approximately 90) and discuss the assignment of mode numbers further. The assignment of the longitudinal quantum number, n_z , on the basis of the one-dimensional Schrodinger equation is particularly tricky, as the existence of cap modes forces nodes in the bulk-mode functions near the caps and prevents accurate fitting of the lowest-few bulk modes to a sinusoidal form, $\sin(k_z z)$, with k_z strictly equal to π/h times an integer. Nevertheless, an unambiguous labeling of the modes is possible.

In Sec. V, we show that the mode frequencies we obtain agree surprisingly well with the Herring-Kittel expression (3), provided we identify k_\perp and k_z in this formula correctly. We give reasons why this agreement might be so good and explain how the wavevector components are found and how this allows us to organize the normal-mode spectrum into families of modes labeled by p .

Spatial patterns for a variety of modes are given in Secs. VI and VII (in Figs. 11–18 and 20). These patterns are the centerpiece of our paper and show beautiful regularity and symmetry. In Sec. VI, we consider only the $d = 75$ nm $h = 300$ nm sample, while, in Sec. VII, we consider the lowest-three $p = 0$ modes as a function of h . We find that, at small h/d (disklike sample), the symmetric cap mode (which has the lowest frequency of all three) is, in fact, the mode that one would regard as the uniform FMR or Kittel mode, and its frequency fits well with the Kittel formula with an appropriate choice of demagnetization coefficients. For large h/d , however, it is the lowest bulk mode (the frequency of which lies above the two cap modes) that should be identified with the Kittel mode. For intermediate values of $h/d \simeq 6$ –8, the Kittel formula does not actually describe any of the modes. This point has not been appreciated before. Once again, it illustrates the richness of the normal-mode spectrum in nonellipsoidal samples.

Finally, Sec. VIII summarizes our conclusions. Here, we take the opportunity to emphasize the importance that simulations of the small-amplitude mode structure in nanostructures have for present and possible future applications, some of which are currently speculative in character.

II. MODES IN THE EXCHANGE-DOMINATED LIMIT

In the presence of an isotropic exchange interaction, and neglecting the effects of damping, Eq. (1) takes the form [24]

$$\begin{aligned} \frac{d\mathbf{M}}{dt} &= -\gamma \mathbf{M} \times \left(\mathbf{H} - \frac{2A_{\text{ex}}}{M_0^2} \nabla^2 \mathbf{M} \right), \\ &= -\gamma \mathbf{M} \times \left(\mathbf{H} - \frac{D_{\text{ex}}}{M_0} \nabla^2 \mathbf{M} \right), \end{aligned} \quad (5)$$

where A_{ex} is a parameter fixing the strength of the exchange interaction and $D_{\text{ex}} \equiv 2A_{\text{ex}}/M_0$. Here, \mathbf{H} is the applied magnetic field, $H_0 \hat{\mathbf{z}}$, plus the dipolar or demagnetizing field generated by \mathbf{M} . In a cylinder of finite height, the dipolar field is not uniform, especially near the caps, and thus, the static equilibrium field, $\mathbf{M}_{\text{eq}}(\mathbf{r})$, is not everywhere parallel to $\hat{\mathbf{z}}$. A linearized normal-mode analysis should, therefore, consider deviations, $\delta \mathbf{M}(\mathbf{r}, t) \perp \mathbf{M}_{\text{eq}}$, that do not lie in the x - y plane. If exchange is strong, however, the nonuniformity in \mathbf{M}_{eq} is very small (this is true for all the simulations we perform), and we may then take $\delta \mathbf{M}_z = 0$. This assumption makes it much easier to discuss

the physics, and relaxing it only obscures the key ideas without adding substance. We stress that it is not essential to our argument, especially with respect to the symmetries and the azimuthal quantum number. With this assumption, we may write

$$\mathbf{M}(\mathbf{r}, t) = M_0[(1 - m^2)^{1/2} \hat{\mathbf{z}} + \mathbf{m}(\mathbf{r}, t)], \quad (6)$$

where \mathbf{m} has only x and y components and is dimensionless, since we have scaled out M_0 .

For small deviations, $|\mathbf{m}| \ll 1$, the linearized LL equation can be cast as

$$\begin{aligned} \frac{d\mathbf{m}(\mathbf{r}, t)}{dt} &= \gamma \hat{\mathbf{z}} \times [H_z(\mathbf{r}, z) \mathbf{m}(\mathbf{r}, t) - M_0 \mathbf{h}_d(\mathbf{r}, t) \\ &\quad - D_{\text{ex}} \nabla^2 \mathbf{m}(\mathbf{r}, t)]. \end{aligned} \quad (7)$$

Here, $H_z(\mathbf{r}, z)$ consists of the applied field, $H_0 \hat{\mathbf{z}}$, together with the position-dependent longitudinal demagnetization field arising from the static magnetization, and \mathbf{h}_d is the (small) demagnetization field induced by \mathbf{m} . (We use cylindrical coordinates $\mathbf{r} = (r, \varphi, z)$ here and below.)

A. Assignment of the angular-momentum quantum number

Equation (7) defines an eigenvalue problem with cylindrical symmetry, so there must exist solutions with a definite azimuthal-mode number. In the zero-exchange or magnetostatic limit, the analysis is best done in terms of a *scalar* magnetic potential, ψ , which varies as $e^{im\varphi}$ in the eigenmodes; the integer m (which we must be careful to distinguish from the scalar value of \mathbf{m}) is then naturally interpreted as the angular-momentum quantum number. In the strong-exchange limit, the problem is better formulated in terms of \mathbf{m} directly, which as a *vector* field transforms differently under rotations than a scalar field [25] [such as $\psi(\mathbf{r})$ in the Schrodinger equation].

Let us examine the effect of a rotation on the vector \mathbf{m} at a point (x, y, z) by an angle ε about the z axis to a vector \mathbf{m}' at the point (x', y', z) . We need only carry this analysis out to leading order in ε . The components of the rotated vector \mathbf{m}' are then (see Fig. 1)

$$m'_x(x', y', z) = m_x(x, y, z) - \varepsilon m_y(x, y, z), \quad (8a)$$

$$m'_y(x', y', z) = \varepsilon m_x(x, y, z) + m_y(x, y, z). \quad (8b)$$

The coordinates (x', y', z) themselves are related to (x, y, z) by

$$x' = x \cos \varepsilon + y \sin \varepsilon = x - \varepsilon y, \quad (9a)$$

$$y' = y \cos \varepsilon + x \sin \varepsilon = y + \varepsilon x. \quad (9b)$$

If we expand the left side of Eq. (8) to first order in ε , note that to zeroth order $\mathbf{m}'(x', y', z) = \mathbf{m}(x, y, z)$, and

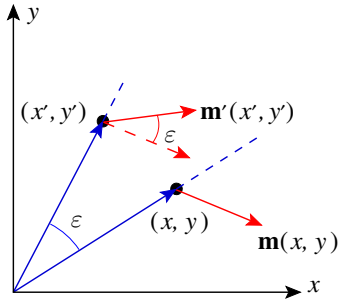


FIG. 1. Transformation of a vector field.

recall the definition of the (dimensionless) orbital angular-momentum operator, l_z , in quantum mechanics as

$$l_z = -i \left(x \frac{\partial}{\partial y} - y \frac{\partial}{\partial x} \right) = -i \frac{\partial}{\partial \varphi}, \quad (10)$$

we can write \mathbf{m}' in terms of \mathbf{m} as

$$m'_x(x, y, z) = (1 - i\varepsilon l_z)m_x(x, y, z) - i\varepsilon[-im_y(x, y, z)], \quad (11a)$$

$$m'_y(x, y, z) = (1 - i\varepsilon l_z)m_y(x, y, z) - i\varepsilon[im_x(x, y, z)]. \quad (11b)$$

Equation (11) can be rewritten in the form

$$\begin{pmatrix} m'_x \\ m'_y \end{pmatrix} = \begin{pmatrix} 1 - i\varepsilon l_z & 0 \\ 0 & 1 - i\varepsilon l_z \end{pmatrix} \begin{pmatrix} m_x \\ m_y \end{pmatrix} - i\varepsilon \begin{pmatrix} 0 & -i \\ i & 0 \end{pmatrix} \times \begin{pmatrix} m_x \\ m_y \end{pmatrix}. \quad (12)$$

For a *scalar* field, $\psi(\mathbf{r})$, we simply have $\psi'(\mathbf{r}) = (1 - i\varepsilon l_z)\psi(\mathbf{r})$, but the presence of the last term in Eq. (12) *mixes* the two components of the *vector* field \mathbf{m} . This can be interpreted as arising from an “internal” or “spin” angular momentum of $m_s = \pm 1$ that is added to or subtracted from the orbital angular momentum, m_l , associated with our vector field \mathbf{m} (a tensor of rank 1). A similar separation exists in the description of light fields [26].

Consider the case of a vector field of the form

$$m_x(\mathbf{r}) = a(r, z)e^{ip\varphi}, \quad m_y(\mathbf{r}) = b(r, z)e^{ip\varphi}, \quad (13)$$

where a and b are arbitrary functions. This field has orbital angular momentum $m_l \equiv p$, but has no definite spin angular momentum. For it to have a definite spin, a and b must

be proportional, according to

$$\begin{pmatrix} m_x \\ m_y \end{pmatrix} \propto \begin{pmatrix} 1 \\ i \end{pmatrix} \Leftrightarrow m_s = 1 \quad \text{or} \quad \begin{pmatrix} m_x \\ m_y \end{pmatrix} \propto \begin{pmatrix} 1 \\ -i \end{pmatrix} \Leftrightarrow m_s = -1. \quad (14a,b)$$

Writing $m_{\pm} = m_x \pm im_y$, it then follows that

$$m_s = 1 \text{ yields } m_+ = 0, \quad m_- \propto e^{ip\varphi}, \quad \text{and } m_{\text{tot}} = p + 1, \quad (15a)$$

and

$$m_s = -1 \text{ yields } m_+ \propto e^{ip\varphi}, \quad m_- = 0, \quad \text{and } m_{\text{tot}} = p - 1, \quad (15b)$$

where we write $m_{\text{tot}} = m_l + m_s$. It follows that an eigenmode with total angular momentum $p + 1$ must be of the form

$$\begin{bmatrix} m_x(\mathbf{r}, t) \\ m_y(\mathbf{r}, t) \end{bmatrix} = F_-(r, z) \begin{pmatrix} 1 \\ i \end{pmatrix} e^{i(p\varphi - \omega t)} + F_+(r, z) \begin{pmatrix} 1 \\ -i \end{pmatrix} e^{i[(p+2)\varphi - \omega t]}, \quad (16)$$

where we adopt an $e^{-i\omega t}$ time dependence, following standard practice. The physical solution is obtained by taking the real part of this complex-valued solution. We shall see below that, for positive-frequency solutions, $F_- \gg F_+$ in the strong-exchange limit, and it is often convenient to neglect F_+ entirely. It is then more useful to label the modes by p , the orbital angular momentum of the dominant component, F_- . This is especially so when looking at mode patterns generated by OOMMF, since we can read off p by seeing how many times \mathbf{m} turns, as we go around a circle in the x - y plane. For example, in a $p = 0$ mode [see Figs. 11(a) and 11(b)], \mathbf{m} appears uniform, while in $p = -1$ (Fig. 13) and $p = 1$ (Fig. 14) modes, \mathbf{m} winds by 2π and -2π , respectively as we go anticlockwise around a circle.

In the magnetostatic limit by contrast, $F_+/F_- \sim O(1)$, and the m labeling is better. Thus, for the sphere, while we would describe the uniform or Kittel mode as having $p = 0$, Walker assigns $m = 1$ to it [see Fig 3 of Ref. [19] where the mode is labeled (110)].

B. Near degeneracy of p and $-p$ modes

When exchange dominates over dipole-dipole interactions, we may, as a first approximation, neglect \mathbf{h}_d in

Eq. (7). In component form, the equation then reads

$$\frac{d}{dt} \begin{bmatrix} m_x(\mathbf{r}, t) \\ m_y(\mathbf{r}, t) \end{bmatrix} = \gamma [H(r, z) - D_{\text{ex}} \nabla^2] \begin{bmatrix} -m_y(\mathbf{r}, t) \\ m_x(\mathbf{r}, t) \end{bmatrix}, \quad (17)$$

or

$$\frac{d}{dt} m_{\pm}(\mathbf{r}, t) = \pm i\gamma [H(r, z) - D_{\text{ex}} \nabla^2] m_{\pm}(\mathbf{r}, t), \quad (18)$$

with

$$m_{\pm}(\mathbf{r}, t) = m_x(\mathbf{r}, t) \pm im_y(\mathbf{r}, t). \quad (19)$$

We seek solutions of the form

$$m_{\pm}(\mathbf{r}, t) = m_{\pm}(\mathbf{r}) e^{-i\omega t}, \quad (20)$$

and demand that $\omega > 0$, with the understanding that the physical solution will be given by the real part. These solutions then obey

$$\gamma [H_z(r, z) - D_{\text{ex}} \nabla^2] m_{\pm}(\mathbf{r}) = \mp \omega m_{\pm}(\mathbf{r}). \quad (21)$$

This equation is like a one-particle Schrodinger equation and, since $\gamma > 0$ in our convention, the operator on the left is a positive operator, which cannot have negative eigenvalues. Since we also demand that $\omega > 0$, we must choose $m_+ = 0$. Finally, since our finite cylinder retains full azimuthal symmetry, the solution for m_- takes the form $m_-(r, \varphi, z) = F_-(r, z) e^{ip\varphi}$, where $F_-(r, z)$ can be chosen to be real, and ω has the same (positive) value for either sign of p . In terms of the general form (16), this solution corresponds to putting $F_+ = 0$, and a physical solution

$$\begin{aligned} \begin{bmatrix} m_x(\mathbf{r}, t) \\ m_y(\mathbf{r}, t) \end{bmatrix} &= F_-(r, z) \begin{pmatrix} 1 \\ i \end{pmatrix} e^{i(p\varphi - \omega t)} + \text{c.c.} \\ &= 2F_-(r, z) \begin{bmatrix} \cos(p\varphi - \omega t) \\ \sin(p\varphi - \omega t) \end{bmatrix}. \end{aligned} \quad (22)$$

If we now include the dipolar field, \mathbf{h}_d , as a perturbation, we can expect that F_+ will become nonzero, with $F_+/F_- \sim 4\pi M_0/D_{\text{ex}} k^2$, where $2\pi/k$ is the typical length scale on which the solution varies.

The source of the degeneracy with respect to $\pm p$ is that Eq. (17) is invariant under reflection in the y - z plane, provided we do not also reflect the vector \mathbf{m} . Hence, the operations $m_x(x, y, z) \rightarrow m_x(-x, y, z)$ and $m_y(x, y, z) \rightarrow m_y(-x, y, z)$ also produce a solution. This operation is equivalent to $\varphi \rightarrow -\varphi$ or alternatively to $p \rightarrow -p$. Inclusion of the dipole-dipole interaction destroys this invariance: the field \mathbf{h}_d produced by the operation is not the same field as before.

Strictly speaking, therefore, modes differing only in the sign of p are not degenerate, although the nondegeneracy

may be small. Indeed, as explained below, we have spent significant effort in numerically resolving the splitting and have not always succeeded. The physical origin of this nondegeneracy is just that the applied external field breaks time-reversal and parity symmetries. In the magnetostatic limit, this point emerges directly from the solution in terms of the scalar potential. Joseph and Schlomann [27] find that $\omega_{-|m|} > \omega_{|m|}$ for the volume modes (where we here use m instead of p to label the modes) and that only $m > 0$ solutions exist for the surface modes. This is an extreme form of the nondegeneracy and is the cylindrical analog of Damon and Eshbach's [28] discovery of one-sided surface modes in the slab geometry. Joseph and Schlomann also find that the $\pm p$ splitting becomes smaller with increasing k_z or increasing radial mode number (see Fig. 5 of Ref. [20]). The same behavior is found for the general spheroid by Walker [29]. Arias and Mills, on the other hand, appear to us to be finding that modes with opposite sign of angular momentum are degenerate; we are unable to pinpoint why.

The near degeneracy of $\pm p$ modes also underlies whether one sees azimuthal standing- or running-wave patterns in the OOMMF simulations. We discuss this issue in Sec. III C.

C. The long cylinder in the exchange-dominated approximation

For an infinite cylinder, the variables in the Schrodinger equation separate, and we can write

$$\begin{aligned} F_-(r, z) &= m_0 J_p(k_{\perp} r) \{A \cos[k_z(z - h/2)] \\ &\quad + B \sin[k_z(z - h/2)]\}, \end{aligned} \quad (23)$$

yielding

$$\begin{aligned} \begin{bmatrix} m_x(\mathbf{r}, t) \\ m_y(\mathbf{r}, t) \end{bmatrix} &= m_0 J_p(k_{\perp} r) \{A \cos[k_z(z - h/2)] \\ &\quad + B \sin[k_z(z - h/2)]\} \begin{bmatrix} \cos(p\phi - \omega t) \\ -\sin(p\phi - \omega t) \end{bmatrix}. \end{aligned} \quad (24)$$

Here, J_p is the Bessel function of order p . For a long but finite cylinder, Eq. (23) should be a good approximation, except for the cap modes.

If we take the modes $+p$ and $-p$ as degenerate, we can superimpose them and form standing waves in φ , an operation we carry out in the next section. Inserting any of these forms into Eq. (12) yields the frequencies

$$\omega = \gamma [H_0 + D_{\text{ex}} (k_z^2 + k_{\perp}^2)]. \quad (25)$$

If we adopt the boundary condition (discussed below)

$$\left(\mathbf{n} \cdot \frac{d}{dr} \right) \mathbf{m} = 0, \quad (26)$$

where \mathbf{n} is a vector normal to the surface, the values of k_{\perp} will be fixed by the condition

$$\frac{dJ_p(k_{\perp}a)}{dk_{\perp}} = 0, \quad (27)$$

where a is the cylinder radius. We write the solutions of Eq. (27) as k_{p,n_r} , where n_r denotes the number of additional zeros of J_p (other than those for $J_{p \neq 0}$ at $r=0$) within the cylinder of radius a . We find that Eq. (27) agrees quite well with the simulations.

For the finite cylinder, we present the argument in two stages. In the first stage, we assume that the inhomogeneity in the static demagnetization field can be ignored and take $H(r, z) = H_0 - 4\pi N_{\parallel} M_0$, with N_{\parallel} being the longitudinal demagnetization coefficient. The solution (25) continues to hold, but the mode frequencies are given by

$$\omega(k_z, k_{\perp}) = \gamma[H_0 - 4\pi N_{\parallel} M_0 + D_{\text{ex}}(k_z^2 + k_{\perp}^2)]. \quad (28)$$

The allowed values of k_{\perp} are given by k_{p,n_r} , as discussed above, but the quantization of k_z is less simple. If the end caps are taken to be at $z=0$ and $z=h$, then to have definite parity under reflection in the mid plane at $z=h/2$, the mode function must depend on z as either $\cos[k_z(z-h/2)]$ (even parity) or $\sin[k_z(z-h/2)]$ (odd parity), but the association between k_z and parity depends on the boundary condition applied at the caps.

If the boundary condition is taken as $(\mathbf{n} \cdot \nabla)\mathbf{m} = 0$, then the allowed k_z values are

$$k_z = \frac{\pi}{h}v_z, \quad v_z = 0, 1, 2, \dots \quad (29)$$

Even parity is associated with even v_z and odd parity with odd v_z .

If instead the boundary condition is taken as $\mathbf{m} = 0$, the allowed values of k_z are

$$k_z = \frac{\pi}{h}v_z, \quad v_z = 1, 2, \dots \quad (30)$$

Now even parity is associated with odd v_z and odd parity with even v_z .

The boundary condition obeyed by OOMMF mode functions is closer to $(\mathbf{n} \cdot \nabla)\mathbf{m} = 0$ than to $\mathbf{m} = 0$. In addition, they do have definite parity. Except for the two lowest-frequency modes, which we call cap modes and which require a separate discussion, they are well fitted by the $\cos[k_z(z-h/2)]$ and $\sin[k_z(z-h/2)]$ forms. However, it is advantageous to allow for a shift and write

$$k_z = \frac{\pi}{h}v'_z, \quad (31)$$

where

$$v'_z = v_z + \delta v_z \quad (v_z \geq 2). \quad (32)$$

We can refer to δv_z as an ‘‘end defect,’’ analogous to the concept of a quantum defect in atomic spectroscopy [30]. With this correction, Eq. (28) continues to be a good approximation for the mode frequencies.

We comment further on the boundary condition, Eq. (26), that the normal derivative vanishes at the surface. The isotropic continuum exchange field, $-D_{\text{ex}}\nabla^2 M$, arises from a microscopic $\mathbf{S}_i \cdot \mathbf{S}_j$ Heisenberg interaction, which has the property that, for any pair of spins, the torque on \mathbf{S}_i due to \mathbf{S}_j cancels that on \mathbf{S}_j due to \mathbf{S}_i . Thus, the total exchange torque on the body vanishes and Eq. (26) is the continuum expression of this fact. This argument dates back to Ament and Rado [31] and has been used by many authors since. Aharoni [32] offers a different derivation. Thus, it would appear to be very general and valid for any D_{ex} , however small. For the magnetostatic limit, $D_{\text{ex}} = 0$, there is, however, no such condition on \mathbf{M} . Turning on D_{ex} perturbatively would then appear to lead to a contradiction. This is not so for the following reason.

In the boundary-value problem for the spatial form of the eigenmodes, D_{ex} multiplies the highest derivative and is thus a singular perturbation from the mathematical point of view. Such perturbations are known to lead to thin boundary layers, where the solution changes character rapidly [33]. Thus, while the normal derivative at the surface may formally be zero, there could be large curvature in the boundary layer, and the derivative of \mathbf{m} , as we approach this layer, need not be small. This is especially relevant for our OOMMF simulations, where the discretization into cells may (a) be too coarse to reveal any boundary-layer behavior, and (b) fundamentally preclude measurements of this derivative by fitting to the mode functions. In this case, adoption of an end defect, δv_z , is an effective practical procedure.

D. A variational solution for a cylinder of finite length

In the second stage of our argument, we attempt to include the inhomogeneity in the static demagnetizing field by adopting the trial form

$$m_{\pm}(\mathbf{r}) = Z(z) J_p(k_{\perp}r) \cos(p\varphi). \quad (33)$$

If we substitute this form into Eq. (21), together with some radially averaged z -dependent magnetic field, $\bar{H}(z)$, we obtain the following one-dimensional eigenvalue problem:

$$\omega Z(z) - \gamma \left[\bar{H}(z) - D_{\text{ex}} \left(\frac{d^2}{dx^2} - k_{\perp}^2 \right) \right] Z(z) = 0, \quad (34)$$

with the boundary conditions

$$Z'(0) = Z'(h) = 0. \quad (35)$$

In the spirit of this variational approach, we can obtain $\bar{H}(z)$ by averaging with respect to $J_p^2(k_{\perp}r)$, which will

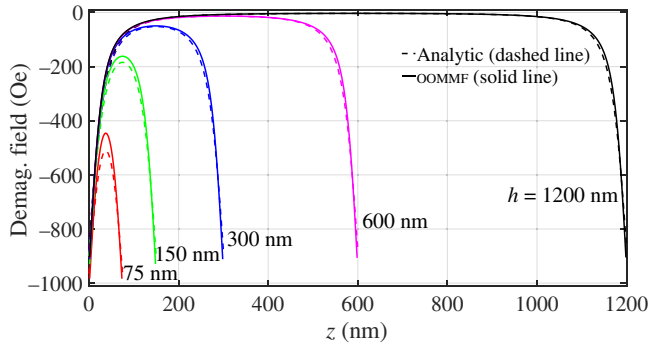


FIG. 2. Dashed lines show the analytical demagnetization field calculated from Eq. (36) using $4\pi M_0 = 1750$ Oe for YIG cylinders with a diameter of 75 nm and five different lengths of 75, 150, 300, 600, and 1200 nm in a field of 2000 Oe. For comparison, the solid lines show the field computed by OOMMF along the line $r=0$. Note how for long cylinders, the field profile near one cap is insensitive to the presence of the other cap.

lead to slight differences between modes with differing k_\perp . Alternatively, we can use the analytical expression for the dipole field along the cylinder axis $H_z(z, r=0)$ that arises from spins which are fully aligned (as expected for the case where exchange is totally dominant) [34]. Assuming a cylinder of radius a and height h , and setting $z=0$ and $z=h$ at the caps, the resulting demagnetization field along the z axis is

$$H_{\text{demag}}(r=0, z) = -2\pi M_0 \times \left[-\frac{h-z}{\sqrt{(h-z)^2 + a^2}} - \frac{z}{\sqrt{z^2 + a^2}} + 2 \right]. \quad (36)$$

In the limit of $a/h \rightarrow 0$, $H_{\text{demag}}(r=0, z) = 0$ (corresponding to an infinite rod), and in the limit of $a/h \rightarrow \infty$, $H_{\text{demag}}(r=0, z) = -4\pi M_0$ (corresponding to a thin disk). Figure 2 shows the resulting magnetic field for YIG cylinders with a diameter of 75 nm and lengths of 75, 150, 300, 600, and 1200 nm as calculated from Eq. (36) (dashed lines) and along the $r=0$ axis by OOMMF. The close correspondence arises from the dominance of exchange in these small-diameter samples.

E. Zeros of mode functions and mode labels

The demagnetizing field plays the role of an external potential in the Schrodinger equation, Eq. (34), and the strong decrease in this field near the end caps leads to surface-bound states or cap states, the wave functions of which die off exponentially away from the caps. In principle, there could be many bound states, but for our parameters we find only one state at each cap. All higher-energy states are extended along the z direction, and since the demagnetization field is essentially uniform in the bulk

TABLE I. Labels for cap and bulk modes.

No. of zeros	Mode label
0	g
1	u
ν_z	$n_z = \nu_z - 2$

of the cylinder, their wave functions behave approximately as sinusoidal standing waves.

Let us now recall that, for a one-dimensional Schrodinger equation with a reflection-symmetric potential, states with successively higher energy alternate in parity and have successively increasing number of zeros, with the lowest-energy state having no nodes and even parity. Furthermore, their wave functions must be mutually orthogonal. For our problem, these theorems are satisfied as follows. The two cap states are nearly degenerate, but they are admixed by tunneling to form even and odd parity states with zero and one node, respectively. (See, however, the discussion in Sec. VII on how the inclusion of dipole-dipole interactions modifies the energy ordering.) The first extended state must then have even parity and two nodes. To be approximated by $\cos[k_z(z-h/2)]$ and to be orthogonal to the cap states, we must have $k_z \lesssim 2\pi/h$, corresponding to $\nu_z = 2$ and a negative end defect, $\delta\nu_z$. Higher extended states must have higher values of ν_z . In this way, we see the need for the restriction $\nu_z \geq 2$ in Eq. (32) and for the end defect at the same time.

For each value of p and n_r , we could label the differently quantized modes along z by the number of zeros. The lowest extended or bulk mode in any family with given p and n_r would then have the label $\nu_z = 2$, while the cap mode will be labeled $\nu_z = 0$. This is unaesthetic and does not differentiate between the physically different characters of the cap modes vis-à-vis the bulk modes. We therefore label the bulk modes by an index n_z , with

$$n_z = \nu_z - 2. \quad (37)$$

For the cap modes, we replace the number n_z by the letters “ g ” (*gerade*, even parity) and “ u ” (*ungerade*, odd parity). For reference, we summarize the correspondence between the number of zeros and the mode labels in Table I.

The modes are labeled by the scheme $(p n_r n_z)$, with the letters g or u for cap modes in lieu of n_z . In particular, the mode nominally identified as the uniform FMR mode has the label (000) (but see the discussion in Sec. VII).

F. Numerical results for the variational approximation and comparison with simulations

We now describe some results from the numerical integration of Eq. (34) together with the position dependence of $H_{\text{demag}}(r=0, z)$ given by Eq. (36). Imposing the boundary condition, Eq. (35), at the faces then yields $Z(z)$

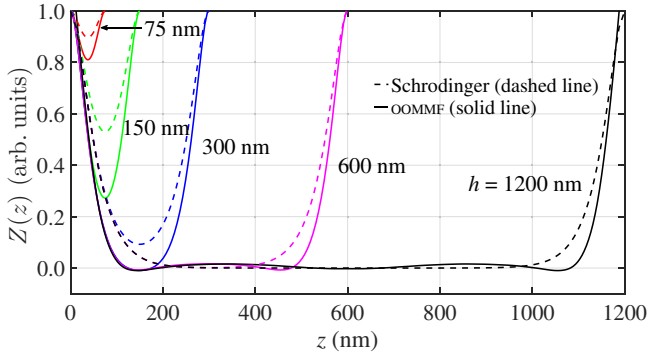


FIG. 3. Dashed lines show the behavior of mode function $Z(z)$ versus z obtained from integrating Eq. (34) for the $(00g)$ cap mode for cylinders with a diameter of 75 nm and heights of 75, 150, 300, 600, and 1200 nm. Solid lines show the OOMMF simulation results for the same parameters.

together with the eigenvalues $\omega = \omega[n_z(p, n_r)]$, where, for the general case, $n_z(p, n_r)$ denotes the eigenvalue for given values of the azimuthal and radial mode numbers, p and n_r , respectively. Given that we neglect the transverse dipolar field to obtain Eq. (34), we expect the resulting eigenvalues to be most accurate in the limit of large n_z mode numbers and, particularly, when both $p = 0$ and $n_r = 0$ [which corresponds to $\theta = 0$ in Eq. (3)].

The dashed lines in Fig. 3 show the resulting form of $Z(z)$ for the lowest-lying cap mode with $p = 0$ and no radial nodes for cylinders with a diameter of 75 nm and heights of 75, 150, 300, 600, and 1200 nm in a field of

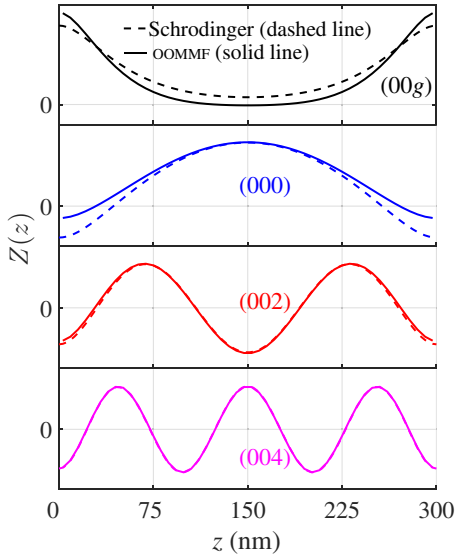


FIG. 4. Dashed lines show mode function $Z(z)$ versus z obtained from integrating Eq. (37) for the $(00g)$, (000) , (002) , and (004) modes. Solid lines show the corresponding forms arising from OOMMF. Note how the behavior at the cylinder faces closely conforms to the boundary condition, Eq. (26).

TABLE II. End defects for $(00n_z)$ modes.

Mode label	ν_z	$hk_{z,\text{fit}}/\pi$	$\delta\nu_z$
000	2	1.62	-0.38
001	3	2.50	-0.50
002	4	3.68	-0.32
003	5	4.78	-0.22
004	6	5.84	-0.16
005	7	6.96	-0.04
006	8	7.90	-0.10
007	9	8.92	-0.08
008	10	10.01	+0.01
009	11	10.91	-0.09
00,11	13	12.96	-0.04
00,13	15	14.98	-0.02
00,15	17	16.92	-0.08

2000 Oe. Notably, the approximately exponential decay of the amplitude as we proceed deep into the interior for longer samples confirms their surface-like character. Also shown are the OOMMF simulations obtained using procedures outlined below (the fact that their amplitudes do not go strictly to zero in longer samples arises from a contamination from other modes). Accompanying antisymmetric modes (not shown) are also highly localized, in addition to having a node at the cylinder midpoint.

As is evident, the semianalytical results for $Z(z)$ are surprisingly good for $h \geq 300$ nm. The frequencies, however, are not. These could be improved by including the transverse dipolar field using perturbation theory, which will raise the frequency. We do not attempt this exercise, since our approximate treatment is quite rough in the first place, and it would not add to our qualitative understanding.

As a crude estimate of the cap-mode frequency, we can compare it with the frequency of a hat box (disk) with a radius equal to its height. Reported demagnetization coefficients [35] for this aspect ratio are $N_{\parallel} = 0.4745$

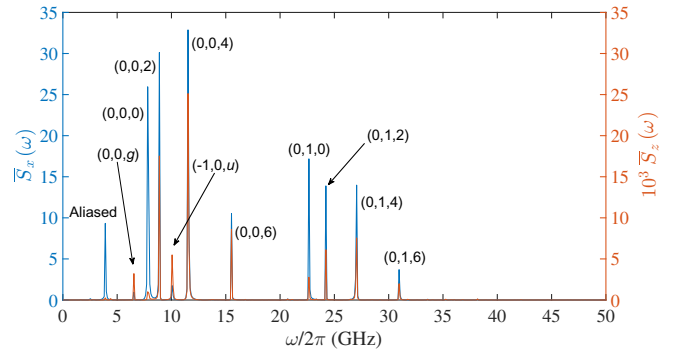


FIG. 5. Example of a FFT spectrum. Left and right y axes show $\tilde{S}_x(\omega)$ and $\tilde{S}_z(\omega)$. Power spectra are given in arbitrary units, but with relative scales for left and right axes as shown. See Eq. (40). A broad sinc pulse, as described in Eq. (38), is used to excite this spectrum.

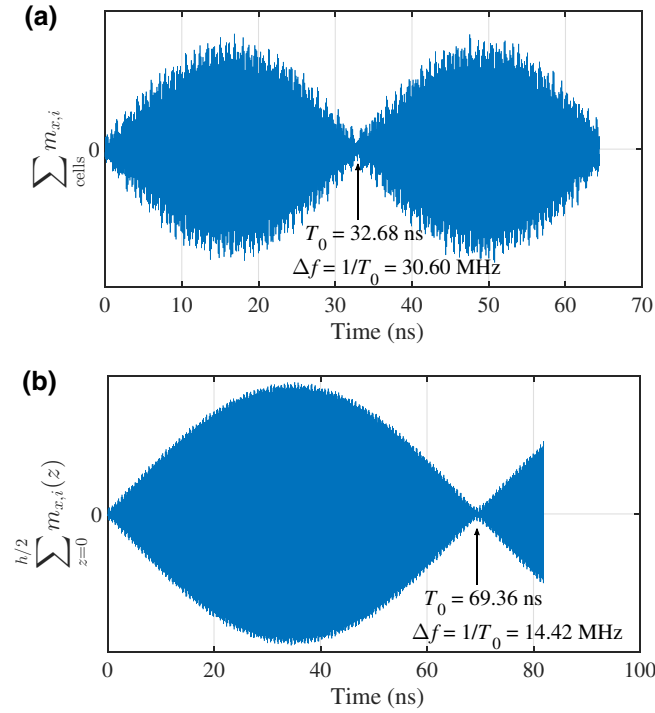


FIG. 6. Beat patterns emerging from the time evolution arising from splitting of (a) the (± 105) modes with an average frequency 17.29 GHz and a splitting of 30.60 MHz, (b) $p = 0$, $n_r = 0$, g and u cap modes with an average frequency of 6.54 GHz and a splitting of 14.4 MHz.

and $N_{\perp} = 0.2628$. For a field of $H_0 = 2.000$ kOe and $4\pi M_0 = 1.750$ kOe, Eq. (2) yields $f = 4.568$ GHz. For our exchange-dominated sample, it is reasonable to add a correction of order $\gamma D_{\text{ex}}/a^2 = 1.0$ GHz, which raises the frequency to 5.6 GHz and is comparable with the OOMMF value of 6.64 GHz. (For our cylinders, $a = 37.5$ nm, and we take $D_{\text{ex}} = 5 \times 10^{-9}$ Oe cm² as is appropriate for YIG.)

Calculations for extended states with mode number $n_z = 0, 1, \dots$ are also performed. Here, we encounter progressively higher mode frequencies, scaling approximately as n_z^2 . Figure 4 shows the results of such calculations for the $(00g)$, (000) , (002) , and (004) modes, according to the designation $(pn_r n_z)$, where p and n_r refer to the azimuthal and radial behavior, which is discussed in Sec. III D, but is absent in this one-dimensional model. Table II lists values of $k_z h/\pi$, v_z , and δv_z for these and neighboring modes. Notably, $\delta v_z \rightarrow 0$ with increasing v_z . We will explain why modes $(00,10)$, $(00,12)$, and $(00,14)$ are not in this table at the end of Sec. III B.

III. COMPUTATIONAL APPROACHES

The material studied here is YIG, which is chosen for its long mode lifetimes. Whether these long lifetimes survive in submicron structures is an open question.

The majority of studies are for a sample with $h = 4d = 300$ nm. The material parameters used are typical for YIG [36]: $\gamma = 2\pi \times 2.8$ GHz/kOe, saturation magnetization $M_s = 139$ emu/cm³, damping constant $\alpha = 5 \times 10^{-5}$, and exchange constant $A_{\text{ex}} = 3.5 \times 10^{-7}$ erg/cm. The applied field is 2 kOe along the z direction. Damping is turned on to relax the system to its initial state and turned off after the system is excited for most simulations. In the few that it is not, it is too small to have any significant effect.

As noted above, our simulations are carried out with the OOMMF code developed by the U.S. National Institute for Standards and Technology. This program divides a chosen sample into cells on a rectilinear grid and numerically integrates the LL equation in time for their magnetizations, $\mathbf{M}_i(t)$, as they evolve under the influence of the torques acting on them arising from an external field, the nearest-neighbor exchange interaction, and the dipolar fields of the remaining cells (anisotropy fields can be included but is ignored in what follows). Each magnetic moment is located at the center of the cell. The number of cells scales with the cube of a characteristic sample dimension but is nominally fixed at $1/54$ cells/nm³, corresponding to a cell size of $3 \times 3 \times 6$ nm³ for the $d = 75$ nm, $h = 300$ nm, sample. There are 50 cells in the z direction and 489 cells in the x - y plane ($489/625 = 0.7824$ vs $\pi/4 = 0.7854$). In Sec. VII, we simulate samples with other values of h . As described there, we then use cells with the same x and y dimensions (3×3 nm²), but depending on the value of h , the dimension Δz is adjusted appropriately.

A. Static equilibrium

Prior to exciting the system, spins are initially aligned along the cylinder axis (parallel to the external field) after which the system is evolved in time (with damping) until it stabilizes in an equilibrium configuration. Various tests can be applied to determine that it is a global equilibrium state. This part of our simulations yields the static magnetic field distribution, which could also be used for the calculations in Sec. II.

B. Exciting the system

Several different excitation schemes are utilized. In the simplest of these, all spins are tipped by a small fixed angle relative to their equilibrium orientations in a plane containing the z axis as an initial condition. This favors the excitation of uniformly precessing modes. To drive a *particular* nonuniform mode, the spins are tipped from their equilibrium positions in a manner that mimics the mode (such as that obtained as the mode pattern in a prior simulation) [37]. To drive a broader *spectrum of modes* that is localized around a time, t_0 , and some position, \mathbf{r}_0 , we tip

TABLE III. Mode frequencies for a YIG cylinder with a height of 300 nm and a diameter of 75 nm in a static magnetic field $\mathbf{H}_0 = 2000$ Oe organized into families with given mode numbers p and n_r . Multiply listed modes [e.g., (-115) and (± 115)] are observed with both pure and mixed $+p$ and $-p$ character, depending on the methodology used to extract them (e.g., FFT versus beat pattern).

p	n_r	n_z	f (GHz)	p	n_r	n_z	f (GHz)	p	n_r	n_z	f (GHz)
0	0	Even cap (g)	6.543	1	0	g	10.35	± 1	0	5	17.29
0	0	Odd cap (u)	6.543	1	0	u	10.35	± 1	0	7	21.78
0	0	0	7.813	1	0	1	11.91	± 1	0	11	33.98
0	0	1	8.105	1	0	3	13.96	± 1	1	g	35.16
0	0	2	8.887	1	0	5	17.29	± 1	1	u	35.16
0	0	3	10.06	1	0	7	21.78	± 1	1	1	36.91
0	0	4	11.52	1	0	9	27.44	± 1	1	3	39.26
0	0	5	13.38	1	0	11	33.98	± 1	1	5	42.68
0	0	6	15.53	1	0	13	41.5	± 1	1	9	52.83
0	0	7	17.97	0	1	0	22.66	± 2	0	g	15.82
0	0	8	20.7	0	1	1	23.24	± 2	0	u	15.82
0	0	9	23.63	0	1	2	24.22	± 2	0	1	18.07
0	0	11	30.27	0	1	3	25.49	± 2	0	2	18.36
0	0	13	37.79	0	1	4	27.05	± 2	0	3	19.63
0	0	15	46.09	0	1	5	28.91	± 2	0	5	22.95
-1	0	g	10.06	0	1	6	30.96	± 2	0	9	33.11
-1	0	u	10.06	0	1	7	33.4	± 2	0	11	39.65
-1	0	1	11.72	0	1	8	36.04	± 2	0	15	55.37
-1	0	2	12.7	0	1	9	38.96	± 3	0	g	24.02
-1	0	3	13.87	0	1	10	42.19	± 3	0	u	24.02
-1	0	4	15.43	0	1	11	45.51	± 3	0	1	25.59
-1	0	5	17.19	0	1	12	49.12	± 3	0	3	27.83
-1	0	6	19.34	-1	1	g	35.16	± 3	0	5	31.25
-1	0	7	21.78	-1	1	u	35.16	± 3	0	7	35.84
-1	0	8	24.41	-1	1	3	39.26	± 3	0	11	47.95
-1	0	9	27.34	-1	1	5	42.68				
-1	0	10	30.57	-1	1	6	44.82				
-1	0	11	33.98	0	2	g	55.57				
-1	0	12	37.6	0	2	0	56.64				
-1	0	13	41.5	0	2	2	58.3				
-1	0	14	45.51	0	2	4	61.23				
-1	0	15	49.71	0	2	6	65.53				
				0	2	8	70.41				

the spins in some direction according to the function

$$F(t, \mathbf{r}) = A \frac{\sin[\Delta\omega(t - t_0)]}{(t - t_0)} \frac{\sin[\Delta k_x(x - x_0)]}{(x - x_0)} \times \frac{\sin[\Delta k_y(y - y_0)]}{(y - y_0)} \frac{\sin[\Delta k_z(z - z_0)]}{(z - z_0)}, \quad (38)$$

where $\Delta\omega$, Δk_x , Δk_y , and Δk_z control the extent to which the excitation is localized in time and space. Here, x , y , and z denote cell coordinates. Such pulses can also be introduced at multiple times and positions to favor the excitation of modes with differing spatial and temporal properties. In particular, the inclusion of only the last factor induces modes propagating along z . Forms can be constructed that favor the excitation of radial or azimuthal modes. Finally, some simulations are performed in which individual spins are tipped in random directions within

some specified average angular range. This excites a very broad range of modes and, if the tipping angles are large (e.g., approaching 180°), generates a “hot” system, from which it is difficult to extract clear modes. Altogether, we have tried more than ten different excitation pulses in an effort to identify modes with different symmetry and numbers of nodes. Despite this, our mode table (see Sec. IV) has gaps. In some cases, modes are nearly degenerate [for example, modes (003) , $(-10g)$, and $(-10u)$] and cannot be easily resolved. In others, they are too high in frequency to be seen with the particular excitation pulse employed. We are confident that these modes exist and that our mode classification is complete.

C. Identifying modes

As the system state simulated by OOMMF evolves in time from some chosen initial configuration, the magne-

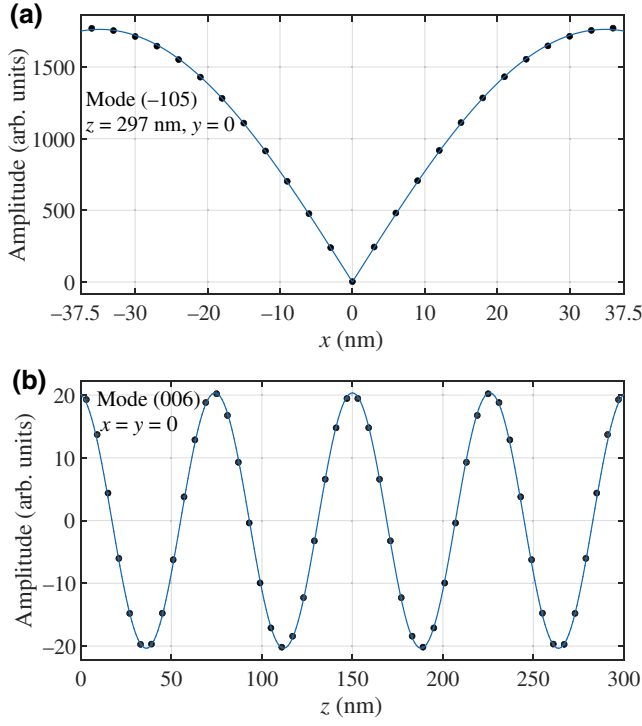


FIG. 7. (a) Typical fit of the radial OOMMF amplitude to the function $J_1(k_\perp r)$ for the (-105) mode. (b) Typical fit of the axial OOMMF amplitude to the function $\cos k_z(z - h/2)$ for the (006) mode.

tization vectors, $\mathbf{m}(\mathbf{r}_i, t)$, at the (discrete) cell sites, \mathbf{r}_i , are recorded at regular time intervals. From this data set, we can perform a cell-by-cell fast Fourier transform (FFT) within some chosen time interval available from the simulation to obtain the complex quantities $\mathbf{m}(\mathbf{r}_i, \omega)$. We stress that the OOMMF simulation does not assume that $\mathbf{M}_{\text{eq}}(\mathbf{r})$ is along $\hat{\mathbf{z}}$ or that the deviations $\mathbf{m}(\mathbf{r}_i, t)$ are in the x - y plane, although the most useful information is contained in these components for low-amplitude mode studies. From

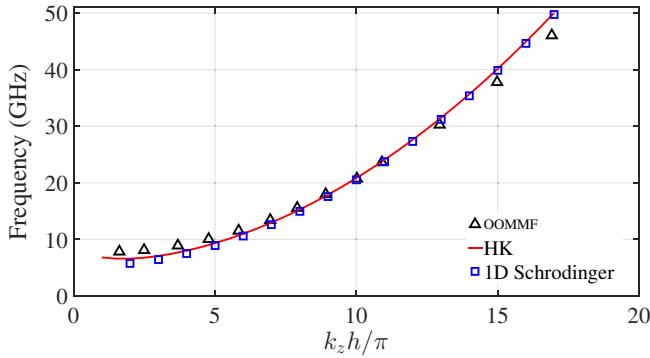


FIG. 8. Frequencies of $(00n_z)$ modes versus k_z , as obtained from OOMMF simulations (triangles), Herring-Kittel formula (solid line), and Schrodinger equation (squares), as discussed in Sec. II B. For Schrodinger equation data, $k_z h / \pi$ is a proxy for $n_z + 2$.

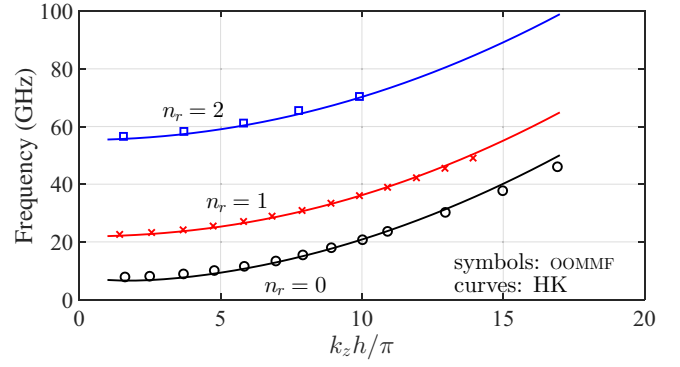


FIG. 9. Symbols show OOMMF simulations for mode frequencies versus dimensionless wavevector k_z for $p=0$ and $n_r=0, 1, \text{ and } 2$; solid lines show predictions of the HK expression.

the FFT, we follow McMichael and Stiles and construct the cell-wise power spectra,

$$S_x(\mathbf{r}_i, \omega) = |m_x(\mathbf{r}_i, \omega)|^2, \quad (39)$$

together with their sum over the entire sample,

$$\bar{S}_x(\omega) = \sum_i S_x(\mathbf{r}_i, \omega), \quad (40)$$

and likewise for $S_y(\mathbf{r}_i, \omega)$ and $\bar{S}_y(\omega)$. As noted by them, this definition of a power spectrum is very different from the power spectrum of the integrated magnetization (total magnetic moment of the sample), which is what makes it so useful in mode identification; in particular, the frequencies where these total sample power spectra have sharp maxima are identified as possible mode frequencies of the system. As an example, the power spectra in Eq. (40) are given in Fig. 5, which shows various modes, including a very-high-frequency mode that is aliased to less than 5 GHz due to a Nyquist critical frequency of 50 GHz.

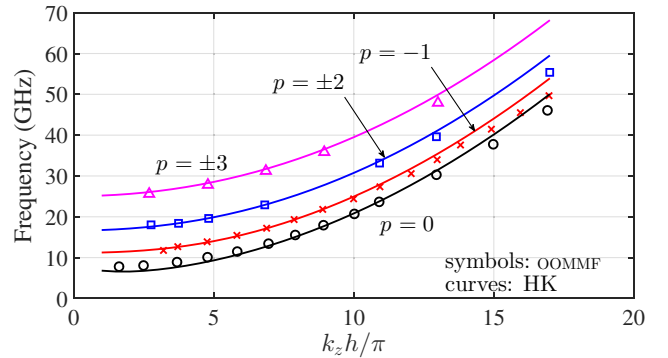


FIG. 10. OOMMF mode frequencies versus k_z for $n_r=0$ and $p=0, -1, \pm 2, \pm 3$. Curves show predictions of the HK equation.

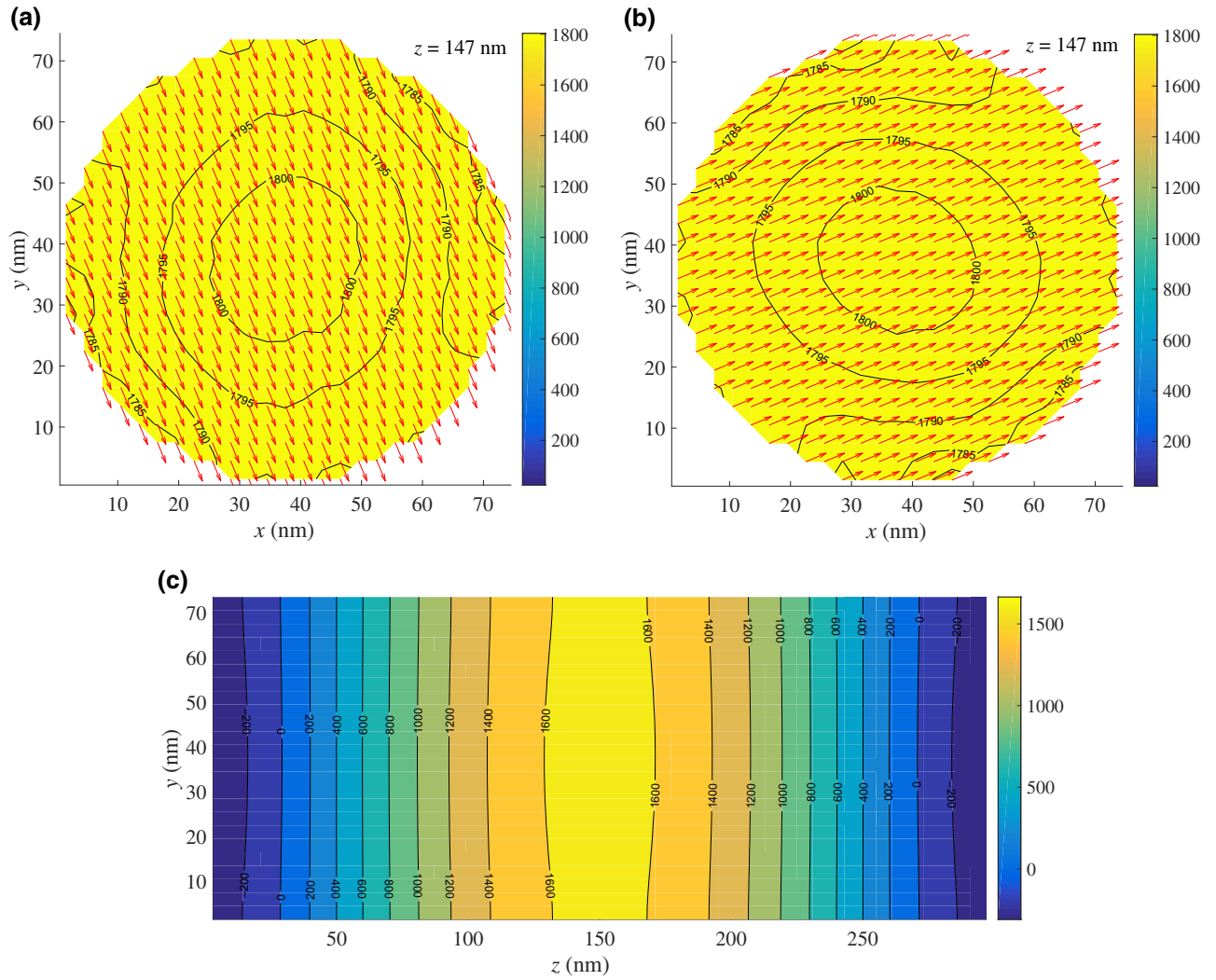


FIG. 11. Mode pattern for lowest (Kittel-like) bulk (000) mode, with a frequency of 7.813 GHz. (a),(b) x - y Cross section of the imaginary and real parts of the Fourier transform amplitude through the cylinder midpoint; (c) real y - z cross section containing the cylinder axis. Arrows show the direction of spins. Spin orientations for the real part correspond to a time $1/4$ cycle later than that for the imaginary part. Lines show contours of constant $|\mathbf{m}(\mathbf{r}, \omega)|$ in (a),(b) and of constant $m_x(\mathbf{r}, \omega)$ in (c); these values are also color coded according to the scale given to the right.

Suppose a mode is identified at a frequency ω_a . With the sign conventions used in our numerical FFT program, the mode pattern associated with this frequency is given by

$$\mathbf{m}^{(a)}(\mathbf{r}_i, t) = \text{Re}[\mathbf{m}(\mathbf{r}_i, \omega)e^{i(\omega_a t + \phi)}]. \quad (41)$$

The phase ϕ is arbitrary and amounts to a choice of the zero of time. To avoid unnecessary minus signs, we choose $\phi = 3\pi/2$, which gives

$$\mathbf{m}^{(a)}(\mathbf{r}_i, 0) = \text{Imm}(\mathbf{r}_i, \omega_a), \quad \mathbf{m}^{(a)}(\mathbf{r}_i, T/4) = \text{Rem}(\mathbf{r}_i, \omega_a), \quad (42)$$

with $T = 2\pi/\omega_a$ being the time period of the mode. Hence, by examining the imaginary and real parts of the vector

$\mathbf{m}(\mathbf{r}_i, \omega_a)$, we can, respectively, obtain the real-space vector magnetization at some time and a quarter-cycle later for the spatial pattern associated with some nominal mode at the specific frequency. By plotting these vector fields, we can get a highly visual depiction of the mode, permitting easy mode assignment and further analysis.

In constructing the power spectrum, modes with higher frequencies than the inverse of the chosen integration time step, which violate the Nyquist sampling criterion and are then aliased to lower frequencies, must be identified and rejected. In the exchange-dominated samples considered here, some of them can be identified as spurious peaks with frequencies lower than the known uniform modes, but, in dipole-dominated larger samples, genuine modes below the uniform modes are expected. More generally,

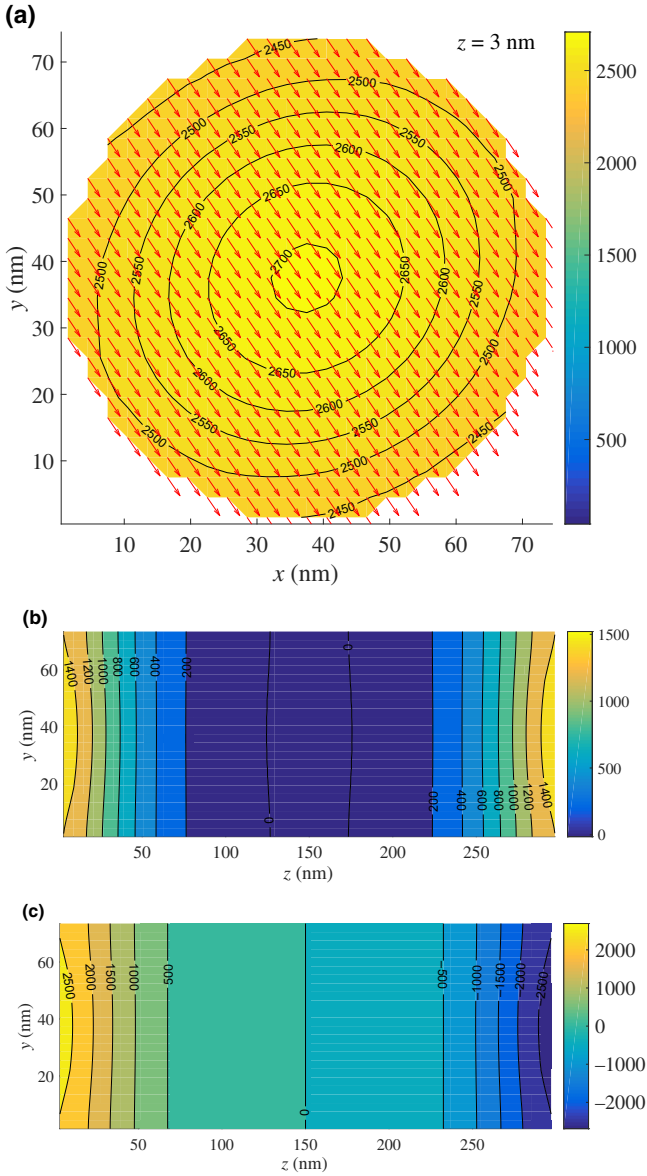


FIG. 12. $p = 0$, $n_r = 0$, cap modes. (a) Real x - y cross section at $z = 0$ of the (00g) symmetric cap mode; this mode has the globally lowest frequency of 6.543 GHz. (b),(c) Real and imaginary y - z cross sections of the g and u modes, respectively, containing the cylinder axis from which surface confinement is apparent.

they must be identified by altering the time interval over which the transform is performed to determine if some mode moves its position. Most simulations are done with a time step of 10 ps and for a duration of 10.24 ns.

A curious spatial aliasing is also observed (as evidenced by a rapid spatial variation of the mode intensity on the scale of the cell period) in some patterns; it is thought to be associated with a spatial FFT that is performed to calculate the dipole field in the underlying program. Such modes must also be rejected.

D. Implications of the $\pm p$ degeneracy for OOMMF patterns

Using the procedures described, we can construct mode maps in chosen planes by plotting the complex cell amplitudes, $\mathbf{m}(\mathbf{r}, \omega) = m_x(\mathbf{r}, \omega)\hat{\mathbf{x}} + m_y(\mathbf{r}, \omega)\hat{\mathbf{y}}$, at frequencies where the power spectrum shows maxima. On the basis of these patterns, we are typically able to assign approximate mode numbers, p , n_r , and n_z , and designate them as $\mathbf{m}^{(pn_r n_z)}[\mathbf{r}, \omega^{(pn_r n_z)}]$ for that frequency, $\omega = \omega^{(pn_r n_z)}$. The p mode number requires special attention, as we now discuss. In what immediately follows, we will drop the mode designation, regarding it as being understood.

Writing the complex function $\mathbf{m}(\mathbf{r}, \omega)$ in component form as

$$\mathbf{m}(\mathbf{r}, \omega) = \begin{bmatrix} m_x(\mathbf{r}, \omega) \\ m_y(\mathbf{r}, \omega) \end{bmatrix} = \begin{bmatrix} m'_x(\mathbf{r}, \omega) + im''_x(\mathbf{r}, \omega) \\ m'_y(\mathbf{r}, \omega) + im''_y(\mathbf{r}, \omega) \end{bmatrix}, \quad (43)$$

the corresponding behavior in the time domain follows as

$$\begin{aligned} \mathbf{m}(\mathbf{r}, t) &= \begin{bmatrix} m_x(\mathbf{r}, t) \\ m_y(\mathbf{r}, t) \end{bmatrix} = \text{Re} \begin{bmatrix} m'_x(\mathbf{r}, \omega) + im''_x(\mathbf{r}, \omega) \\ m'_y(\mathbf{r}, \omega) + im''_y(\mathbf{r}, \omega) \end{bmatrix} e^{-i\omega t}, \\ &= \begin{bmatrix} m'_x(\mathbf{r}, \omega) \cos \omega t + m''_x(\mathbf{r}, \omega) \sin \omega t \\ m'_y(\mathbf{r}, \omega) \cos \omega t + m''_y(\mathbf{r}, \omega) \sin \omega t \end{bmatrix}. \end{aligned} \quad (44)$$

If the modes of the system have a pure p character, as in Eq. (15), we can write the above components as

$$\begin{aligned} m'_x(\mathbf{r}, \omega) &= m(r, z, p, \omega) \cos(p\varphi), \\ m''_x(\mathbf{r}, \omega) &= m(r, z, p, \omega) \sin(p\varphi), \end{aligned} \quad (45a,b)$$

$$\begin{aligned} m'_y(\mathbf{r}, \omega) &= -m(r, z, p, \omega) \sin(p\varphi), \\ m''_y(\mathbf{r}, \omega) &= m(r, z, p, \omega) \cos(p\varphi). \end{aligned} \quad (45c,d)$$

Hence, we can write $\mathbf{m}(\mathbf{r}, t)$ as

$$\begin{aligned} \mathbf{m}(\mathbf{r}, t) &= \begin{bmatrix} m_x(r, z, p, t) \\ m_y(r, z, p, t) \end{bmatrix} = m(r, z, p, \omega) \\ &\times \begin{bmatrix} \cos(p\varphi - \omega t) \\ -\sin(p\varphi - \omega t) \end{bmatrix}. \end{aligned} \quad (46)$$

Here, the magnetization vector rotates as φ changes with a *radially symmetric* amplitude. In our approximation, where the variables r and z separate, we write the solutions

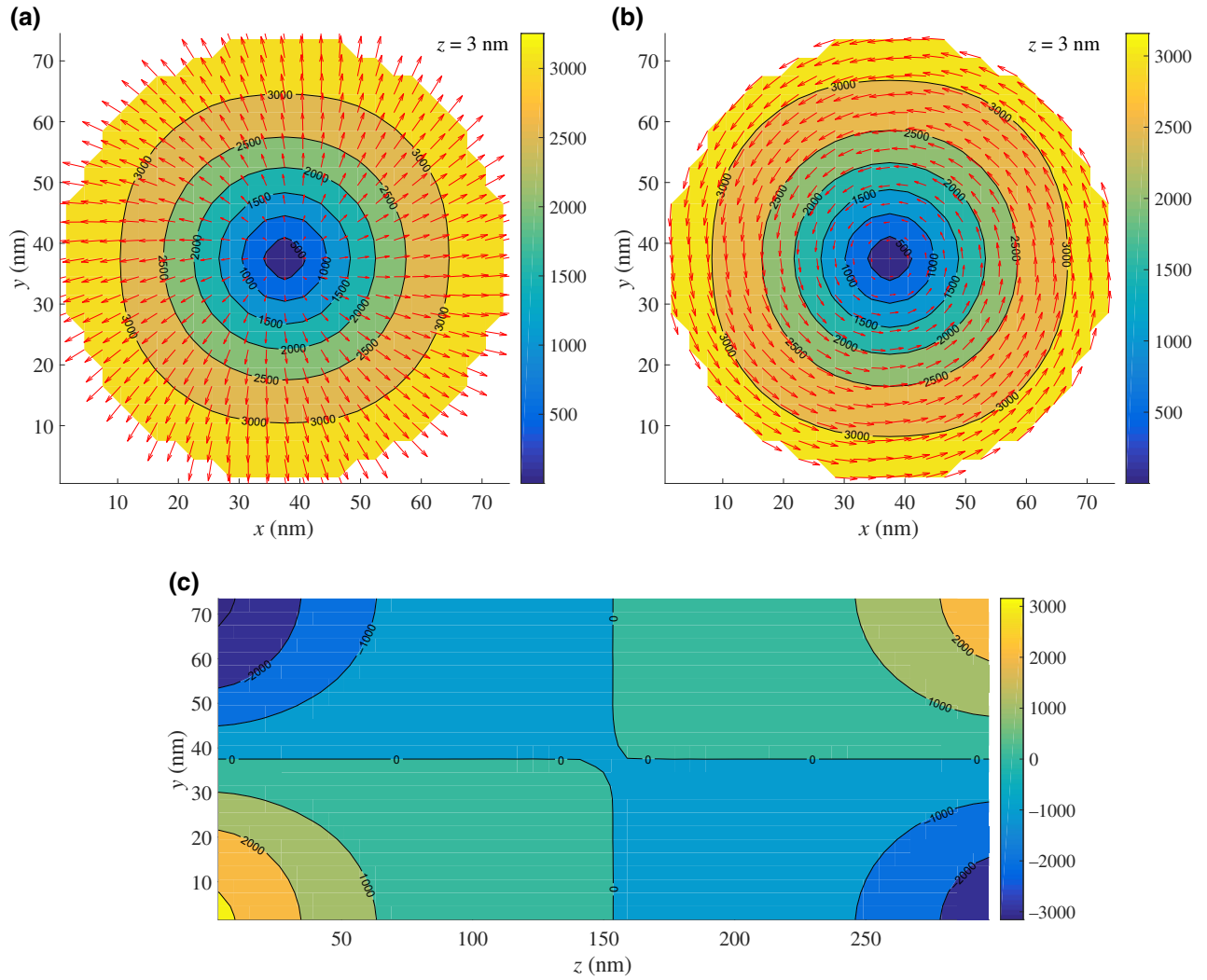


FIG. 13. (a),(b) Imaginary and real x - y cross sections at $z=0$ of $(-10u)$ antisymmetric cap mode with a frequency of 10.06 GHz. (c) Real y - z cross section containing the cylinder axis from which surface confinement is apparent.

that have even parity as

$$\begin{aligned} \begin{bmatrix} m_x(\mathbf{r}, t) \\ m_y(\mathbf{r}, t) \end{bmatrix} &= m_0 \cos[k_z(z - h/2)] J_p(k_\perp r) \\ &\times \begin{bmatrix} \cos(p\varphi - \omega t) \\ -\sin(p\varphi - \omega t) \end{bmatrix}. \end{aligned} \quad (47)$$

If the modes of the system have a pure p character and p and $-p$ are degenerate, we can form symmetric and antisymmetric standing-wave superpositions of the two forms of Eq. (47) to obtain

$$\begin{aligned} \mathbf{m}(\mathbf{r}, t) &= \begin{bmatrix} m_x(r, z, p, t) \pm m_x(r, z, -p, t) \\ m_y(r, z, p, t) \pm m_y(r, z, -p, t) \end{bmatrix}, \\ &= m(r, z, p, \omega) \begin{bmatrix} \cos(p\varphi - \omega t) \pm \cos(-p\varphi - \omega t) \\ -\sin(p\varphi - \omega t) \mp \sin(-p\varphi - \omega t) \end{bmatrix}, \end{aligned} \quad (48)$$

which results in the following two forms:

$$m(r, z, p, \omega) \cos(p\varphi) \begin{bmatrix} \cos(\omega t) \\ \sin(\omega t) \end{bmatrix}, \quad (49a)$$

$$m(r, z, p, \omega) \sin(p\varphi) \begin{bmatrix} \sin(\omega t) \\ -\cos(\omega t) \end{bmatrix}, \quad (49b)$$

or, if our model product form is assumed,

$$m_0 \cos[k_z(z - h/2)] J_p(k_\perp r) \cos(p\varphi) \begin{bmatrix} \cos(\omega t) \\ \sin(\omega t) \end{bmatrix}, \quad (50a)$$

$$m_0 \cos(k_z(z - h/2)) J_p(k_\perp r) \sin(p\varphi) \begin{bmatrix} \sin(\omega t) \\ -\cos(\omega t) \end{bmatrix}. \quad (50b)$$

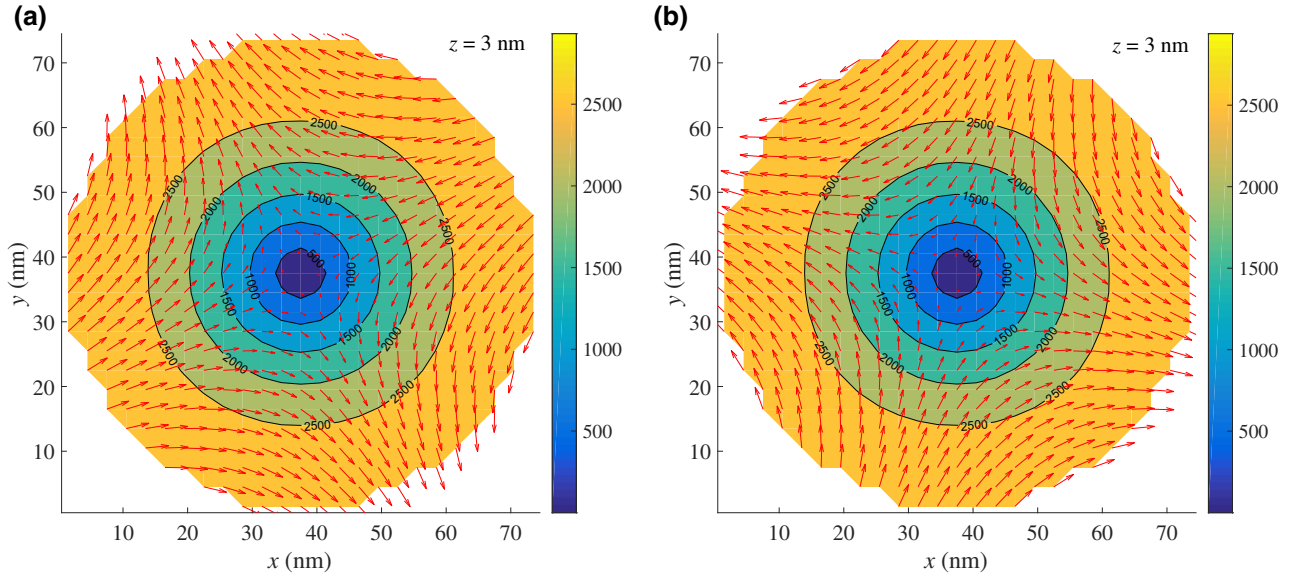


FIG. 14. (a),(b) Imaginary and real x - y cross sections at $z = 0$ of the $(10u)$ antisymmetric cap mode with a frequency of 10.35 GHz. Important to note here is the retrograde character of spin winding.

Here, again the spin direction rotates (in both senses), but now the amplitude is modulated in φ . A similar discussion applies to the solutions that have odd parity.

In Appendix B, we discuss how a pure- p mode pattern can be extracted from a superposition of $+p$ and $-p$ OOMMF patterns.

E. Separating nearly degenerate modes

As noted above, in the absence of the dipole interaction, modes with $+p$ and $-p$ are degenerate. When this interaction is present, such modes are split, i.e., according to the discussion of Sec. III D, our eigenmodes will be running waves in φ . But the splitting rapidly decreases for larger mode numbers, and for running times less than $t \leq \Delta\omega^{-1}$, where $\Delta\omega$ is the splitting, the power spectrum displays a single (slightly broadened) peak at the mode frequency. To resolve the splitting in a power spectrum, the OOMMF run times must be increased.

When the splitting is not resolved in the power spectrum, the resulting mode patterns display a standing-wave character. For a few of these, we use the standing-wave mode pattern as an initial configuration and run the program long enough to display a beat pattern in time from which the splitting can be accurately determined. An example of this technique is shown in Fig. 6 for the cylinder with $d = 75$ nm and $h = 300$ nm. Figure 6(a) shows the case of the (± 105) modes with an average frequency of 17.29 GHz. Note a beat waist occurs at $t = 32.68$ ns from which we calculate the mode splitting as 30.60 MHz.

A very small splitting also occurs between the symmetric (or *gerade*, denoted g) and antisymmetric (*ungerade*, denoted u) combinations of the cap modes. In the Schrodinger equation language of Sec. II, this is a tunnel splitting between the surface-bound states. This splitting is intrinsically small and hard to resolve in long cylinders, although we resolve it for the $p = 0$, $n_r = 0$, g and u cap modes for the cylinder with $h = 300$ nm. Now, $f = 6.54$ GHz and $\Delta f = 14.4$ MHz. The corresponding beat pattern is shown in Fig. 6(b).

IV. FREQUENCIES OF LOW-LYING MODES

Most computations are carried out on a YIG sample with $h = 4d = 8a = 300$ nm in a static field of $H_0 = 2000$ Oe. To test the behavior at small and large k_z , some calculations are carried out for samples with $h = 7.5, 37.5, 75, 150, 600,$ and 1200 nm. The material parameters used are typical for YIG, as given earlier in Sec. III.

Table III lists the frequencies, $f_{p n_r n_z} = \omega_{p n_r n_z} / 2\pi$, of low-lying modes, as obtained from the peaks in the power spectrum; all entries are for $h = 4d = 8a = 300$ nm in a static field of $H_0 = 2000$ Oe. The mode numbers come from a comparison of the accompanying mode pattern with the forms discussed in Sec. II, with special attention paid to the number of radial and longitudinal zeros and how \mathbf{m} winds around the z axis. By fitting to Eq. (25), we can assign discrete wavevectors, k_{\perp, n_r} and k_{n_z} ; these values are used for a comparison with the HK formula, as we describe in the next section. All modes with $p \neq 0$ have a node at $r = 0$; for larger values of k_{\perp} , additional radial nodes can be present and their mode number is denoted as $n_r \neq 0$.

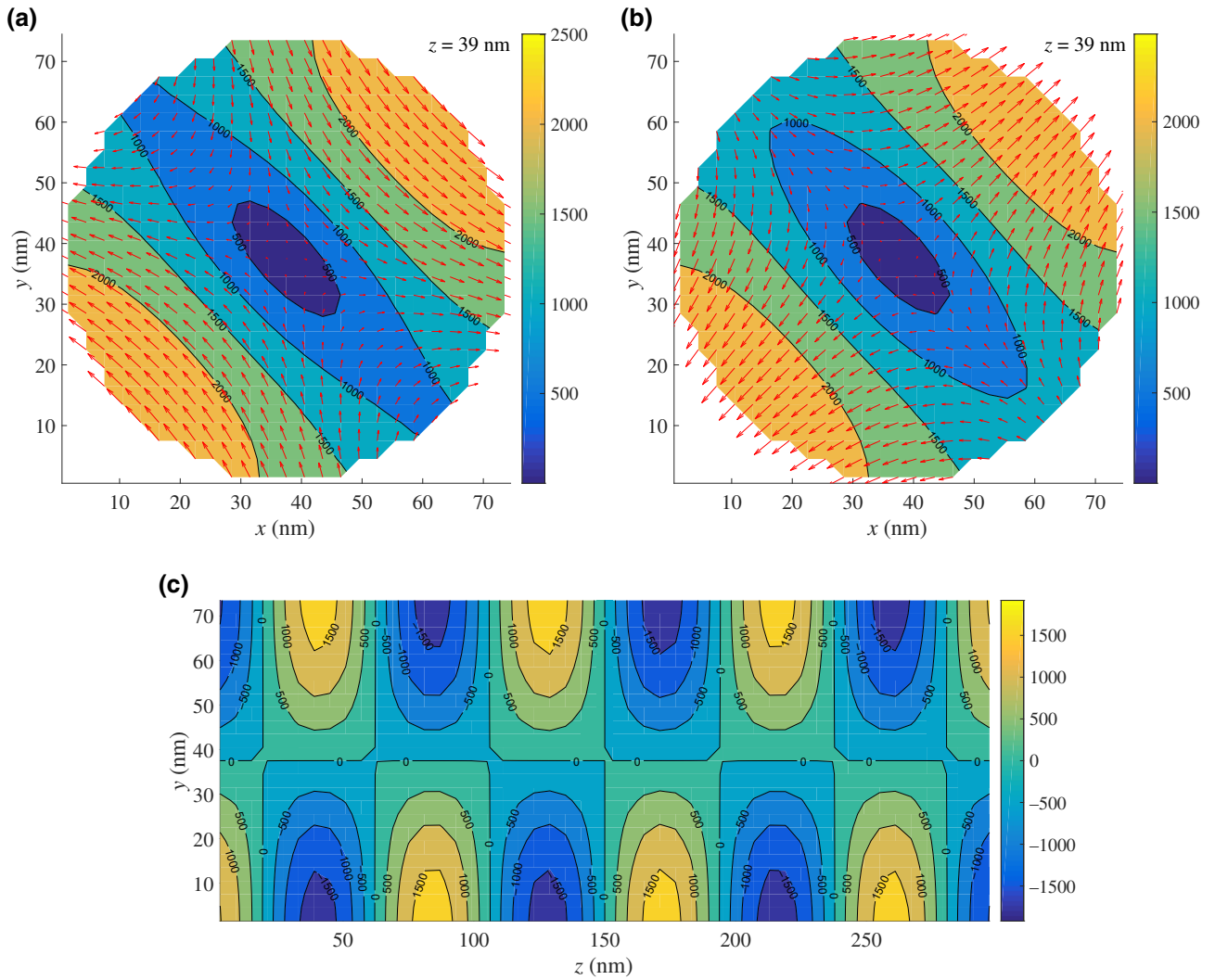


FIG. 15. (a),(b) Imaginary and real x - y cross sections at $z=39$ nm of (± 105) modes with a frequency of 17.29 GHz. Note the standing-wave behavior of these cross sections arising from superposition of azimuthally counterpropagating modes. However, at a fixed point in space, spins still precess counterclockwise. (c) Real y - z cross section containing the cylinder axis.

Modes listed as $\pm p$ are nearly degenerate in the sense discussed above, and the mode patterns display standing waves in φ , as described by Eq. (50 a,b).

V. COMPARISON OF SIMULATED FREQUENCIES WITH THE HERRING-KITTEL EXPRESSION

It is interesting to examine the extent to which the OOMMF mode frequencies in Table III can be represented by the Herring-Kittel frequencies, as given by Eq. (3). To do this, we need values of k_z and k_{p,n_r} for the extended modes. A preliminary value of k_z follows from counting the number of nodes along z . Better values emerge [38] from fitting $m_r(z, r=0, \omega)$ to $\cos[k_z(z-h/2)]$ or $\sin[k_z(z-h/2)]$. Values for $k_{p,n}$ are obtained by fitting $m_r(z, r, \omega)$ to $J_p(k_{p,n}r)$ at some z with $k_{p,n}$ as an adjustable

parameter. Figures 7(a) and 7(b) show examples of such fits. Note that although we do not employ it to find k_z and k_\perp , the boundary condition at the faces for this mode closely approximates the maximum amplitude as opposed to the maximum derivative.

We now show some plots of the frequencies, $f^{(p n_r n_z)} = \omega^{(p n_r n_z)}/2\pi$, inferred from the simulations, for various modes $(p n_r n_z)$ versus k_z at fixed $k_{p,n}$; the latter values are obtained by the above procedures. Also shown are the frequencies predicted by the HK expression, Eq. (3), for the same wavevector components and a demagnetization coefficient of $N_\parallel = 0.098$.

The triangle symbols in Fig. 8 show the results of the OOMMF simulation for the $(00 n_z)$ modes, as a function of k_z in units of π/h , for which the lowest frequency is 7.81 GHz. Not included are the accompanying

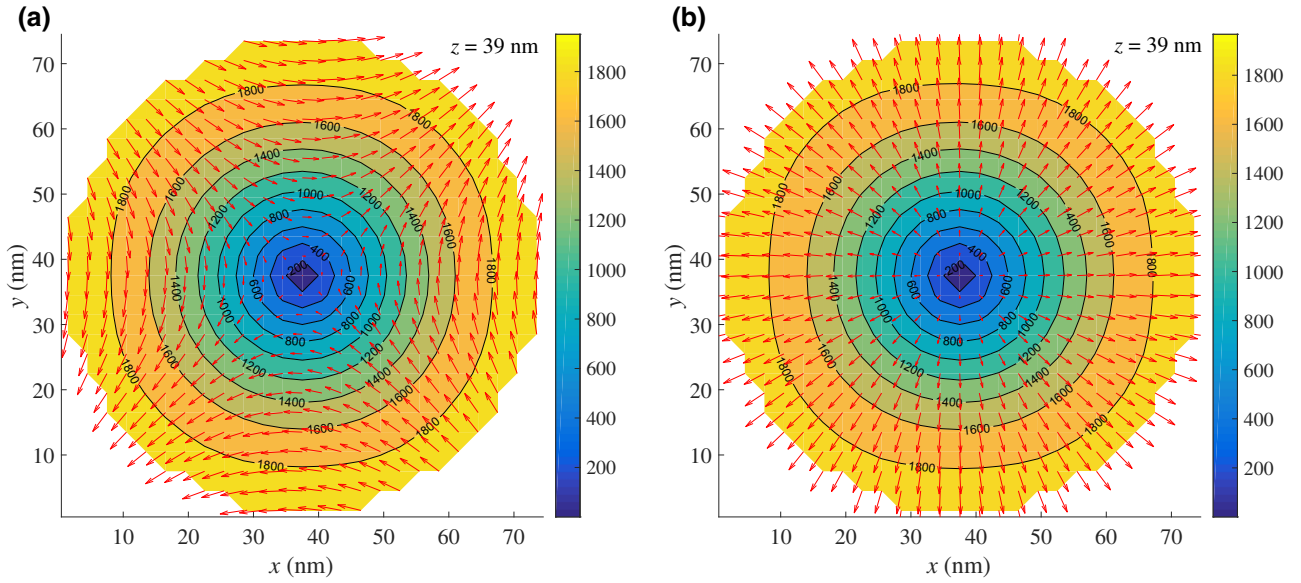


FIG. 16. The projection technique described in Appendix B is used to separate modes with $p = +1$ and $p = -1$ from the same data as that used to construct Fig. 15. Notably, azimuthal intensity is now constant, as appropriate for running waves.

cap-mode frequencies, which are both 6.41 GHz within the resolution. The solid line shows the frequencies predicted by the HK formula. The agreement is surprisingly good, especially at small k_z , where the HK formula is expected to break down. To some extent, this may arise from the fact that the internal magnetic field is position dependent, being lower at the caps, and thereby producing an effect partially compensating that of N_\perp . The square symbols show the predictions of the one-dimensional Schrodinger equation, as described in Sec. II B.

The symbols in Fig. 9 show the OOMMF simulations of $p = 0$ mode frequencies as a function of dimensionless k_z for $n_r = 0, 1$, and 2, while the solid lines show the predictions for the corresponding mode numbers of the HK formula. Again, the agreement is excellent. Readers may notice that some modes are missing from these plots. This is because they are not excited with the protocols used, but we are confident they exist and that their mode patterns conform with the general framework presented here.

Lastly, Fig. 10 shows the OOMMF simulations for mode frequencies versus k_z for $n_r = 0$ and $p = 0, -1, \pm 2, \pm 3 \dots$. The HK formula again gives an excellent overall representation.

Analogous to our approximating the position dependence of the bulk states with a form $\cos(k_z z)$, we can use $e^{-\kappa z}$ and $e^{\kappa(z-h)}$ to qualitatively describe the amplitude in the vicinity of the cylinder faces for the cap modes, i.e., we take k as imaginary by writing $k = i\kappa$, in which case k^2 is replaced by $-\kappa^2$ in a Herring-Kittel-like expression, which pushes the frequency *below* that of the first extended mode.

A. Why the HK formula works so well

The HK relation is sometimes referred to as a spin-wave dispersion relation, and indeed it is tantamount to saying that the normal modes of the body can be described by a continuous (or quasi-continuous) variable, k . As explained in Appendix A, this assertion is grossly incorrect when the spatial variation of \mathbf{m} is on a scale comparable to the dimensions of the body [39]; the mode functions must then take account of the *shape* of the body and be described by discrete sets of appropriate mode numbers, which may or may not be wavevectorlike.

To the extent that some discrete modes with slow spatial variation are well described by wavevectorlike variables, then for those modes the HK expression can be expected to give the frequency to good approximation, especially if one is in the exchange-dominated limit. This is the situation in the present investigation. We see that, for every bulk mode, we can identify a reasonably well-defined k_z and an orbital angular-momentum quantum number, p . We also see a radial dependence in $\mathbf{m}(r)$ that matches a Bessel function well, $J_p(k_\perp r)$, from which can obtain k_\perp .

That the mode functions should look this way is not an accident. We have some support for this functional behavior from the theory of the infinite cylinder in the exchange-dominated limit. We intend to publish details of this theory separately, and here we only summarize the key results. In first-order perturbation in the small parameter,

$$\zeta = \frac{M_0}{D_{\text{ex}} k^2}, \quad (51)$$

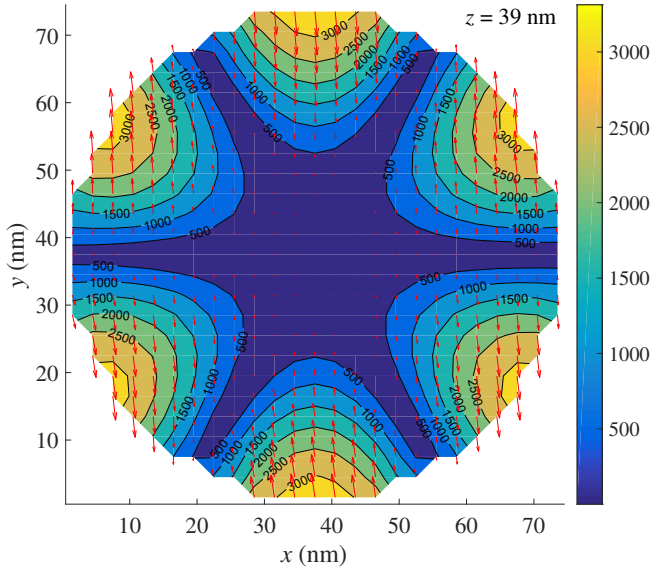


FIG. 17. Real x - y cross section of the (± 305) bulk mode with a frequency of 31.25 GHz, showing multiplicity of azimuthal nodes. Note also the deep central node due to r^3 behavior of $J_3(k_\perp r)$.

we find that the mode function is given by

$$\begin{pmatrix} m_x \\ m_y \end{pmatrix} = \frac{1}{\sqrt{2}} \left\{ [J_p(k_\perp r) + f^-(r)] e^{i(p\varphi - \omega t)} \begin{pmatrix} 1 \\ i \end{pmatrix} + f^+(r) e^{i[(p+2)\varphi - \omega t]} \begin{pmatrix} 1 \\ -i \end{pmatrix} \right\} e^{\pm i k_z z}. \quad (52)$$

The corrections f^\pm are both $O(\zeta)$. We add here that we discovered the properties of the mode functions by experimenting with OOMMF first and developed the theoretical framework later.

VI. EXAMPLES OF MODE PATTERNS

Table III in Section IV lists approximately 90 modes that we can identify. We will now present some accompanying mode patterns that display various behaviors. All figures in this section pertain to YIG cylinders with a diameter $d = 2a = 75$ nm and a height $h = 300$ nm in a magnetic field $H_0 = 2000$ Oe.

There is a wealth of information in these figures, as we now explain. They all depict various aspects of the frequency-space Fourier amplitude, $\mathbf{m}(\mathbf{r}, \omega)$, which is a complex vector, i.e., its x , y , and z components are all complex numbers. The real parts make a vector, and so do the imaginary parts, which we can call the real and imaginary parts of the complex vector, $\text{Re}\mathbf{m}(\mathbf{r}, \omega)$ and $\text{Im}\mathbf{m}(\mathbf{r}, \omega)$. We discard the z component, leaving the x - y projection, $\mathbf{m}_\perp(\mathbf{r}, \omega)$. Circular panels, such as Figs. 11(a) and 11(b), show x - y cross sections of the cylinder, while rectangular panels, such as Fig. 11(c), show y - z cross sections

through a diameter of the cylinder. In the circular panels, the arrows show the directions and relative magnitudes of either $\text{Re}\mathbf{m}_\perp(\mathbf{r}, \omega)$ or $\text{Im}\mathbf{m}_\perp(\mathbf{r}, \omega)$, while the thin black lines show contour levels of the magnitudes of these same vectors, i.e., either $|\text{Re}\mathbf{m}_\perp(\mathbf{r}, \omega)|$ or $|\text{Im}\mathbf{m}_\perp(\mathbf{r}, \omega)|$. These contour levels are also color coded according to the scale on the right. As explained in Sec. III C—see Eqs. (41) and (42)—the Re panel shows the spins a quarter cycle after the Im panel. That is, time proceeds from Im to Re, which is reflected in the sequence of panels (a) and (b) when both Re and Im parts are shown. In the rectangular panels, we show contours of $\text{Re}m_x(\mathbf{r}, \omega)$; again, the contours are color coded. Because the circular panels show the magnitude of the vector in the x - y plane, while the rectangular panels show only the x component, the contour levels in the two types of panels cannot be directly compared. Depending on just how a particular mode is excited, the spins can have larger projections along the x or y directions at the particular time captured in the x - y cross sections, and this can further affect the values of the contour levels in the rectangular panels vis-à-vis the circular ones. If the spins are at 45° to the x and y directions in the x - y cross sections, the values in the rectangular panel will be $2^{-1/2}$ of the circular panels. In general, however, we can only expect these values to be of similar magnitude within a factor of order unity. The most salient feature is the variation or the relative Fourier amplitude within a panel. We add here that our simulations are done with 50 vertical layers of cells of 6 nm high each. There is a layer extending from $z = 144$ to 150 nm and another from $z = 150$ to 156 nm. Hence, circular panels, such as in Figs. 11(a) and 11(b), which are labeled $z = 147$ nm, correspond to the midpoint of the cell layer just below the midplane of the cylinder; panels labeled $z = 3$ nm, such as in Fig. 12(a), show the lowest layer; panels labeled $z = 39$ nm, such as in Figs. 15(a) and 15(b), show the seventh layer from the bottom. However, in the text and figure captions, we describe the panels at $z = 3$ and 147 nm as lying at $z = 0$ and $z = h/2$, respectively, as this is more natural and intuitively easier to understand.

In the interest of clarity, we shall repeat these points as necessary and add further information about the patterns as we discuss them one by one.

We start with the lowest-lying modes: the nominal bulk uniform precession or cylindrical Kittel (000) mode with $f = 7.813$ GHz, which is concentrated within the body of the cylinder, away from the caps, together with the even (00g) and odd (00u) cap modes concentrated on the top and bottom cylinder faces with a mean frequency of 6.543 GHz and a splitting that is too small to be resolved.

Figure 11(a) shows $\text{Im}\mathbf{m}_\perp^{(000)}(x, y, z = h/2, \omega)$, while Fig. 11(b) shows $\text{Re}\mathbf{m}_\perp^{(000)}(x, y, z = h/2, \omega)$ for the (000) bulk mode with $f = 7.813$ GHz; here $\text{Im}\mathbf{m}_\perp(x, y, z = h/2, \omega)$ and $\text{Re}\mathbf{m}_\perp(x, y, z = h/2, \omega)$ denote the normalized vector fields of the Fourier amplitude given by following

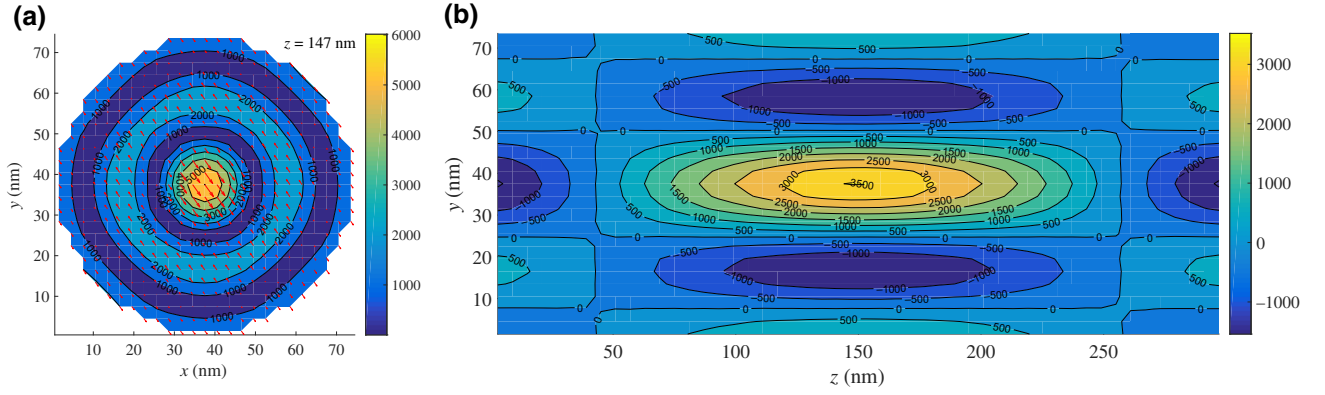


FIG. 18. Real x - y and y - z cross sections of the (020) mode with a frequency of 56.64 GHz exhibiting multiple radial nodes.

prescriptions:

$$\frac{\text{Imm}_{\perp}(\mathbf{r}_i, \omega)}{\left[N_{\text{cell}}^{-1} \sum_i |\text{Imm}(\mathbf{r}_i, \omega)|^2 \right]^{1/2}} K \text{ and} \quad (53)$$

$$\frac{\text{Rem}_{\perp}(\mathbf{r}_i, \omega)}{\left[N_{\text{cell}}^{-1} \sum_i |\text{Rem}(\mathbf{r}_i, \omega)|^2 \right]^{1/2}} K,$$

where K is a global constant scale factor, the value of which is chosen as 1000 for convenience for all mode patterns (this and subsequent ones). The arrows indicate the x - y projection of magnetization. The lines and color coding depict the contours of constant amplitude, either $\text{Rem}_{\perp}(\mathbf{r}_i, \omega)$ or $\text{Imm}_{\perp}(\mathbf{r}_i, \omega)$. Ideally, these would be concentric circles, but there is always contamination at some level from other modes. There may also be numerical errors associated with the discretization. Time proceeds from Im [panel (a)] to Re [panel (b)], a quarter-cycle later.

Figure 11(c) shows $\text{Rem}_x^{(000)}(x=0, y, z, \omega)$, again with contour lines together with color coding. Notably, the contour lines are quite parallel to the faces, a behavior that arises from the strong influence of exchange in these small samples and validates the factorized form of Eq. (23) for $F_-(r, z)$.

Figure 12(a) shows $\text{Rem}_{\perp}^{(00g)}(x, y, z=0, \omega)$ for the symmetric (g) cap mode with $f = 6.543$ GHz. Figures 12(b) and 12(c) show $\text{Rem}_x^{(00g)}(x=0, y, z, \omega)$ and $\text{Imm}_x^{(00u)}(x=0, y, z, \omega)$ for the even (g) and odd (u) cap modes, respectively. We see that the mode intensity is strongly concentrated near the cylinder faces, dropping off rapidly as one proceeds to the interior. Notably, the antisymmetric character of the u mode is clearly apparent, as seen from the node at $z = h/2$.

Figures 13(a) and 13(b) show $\text{Imm}_{\perp}^{(-10u)}(x, y, z=0, \omega)$ and $\text{Rem}_{\perp}^{(-10u)}(x, y, z=0, \omega)$ of the $(-10u)$ antisymmetric 10.06-GHz cap mode, which has a node at $r = 0$. Note

how the spins wind through an angle of 2π as we proceed counterclockwise around the line $r = 0$. Figure 13(c) shows $\text{Rem}_x^{(-10u)}(x=0, y, z, \omega)$, where the antisymmetric behavior in z is evident.

Figures 14(a) and 14(b) show $\text{Imm}_{\perp}^{(10u)}(x, y, z=0, \omega)$ and $\text{Rem}_{\perp}^{(10u)}(x, y, z=0, \omega)$ for the neighboring $p = +1$ mode with a frequency of 10.35 GHz. Here, one encounters the “retrograde” motion associated with the oppositely winding sense of m with the azimuthal angle φ .

We next consider a mode with multiple nodes along z . As remarked upon earlier, the splitting between $\pm p$ modes diminishes as the overall mode number increases, so we designate them with both signs, since our mode-projection method generally yields a superposition. Here, we consider the (± 105) mode(s) with $f = 17.29$ GHz. Figures 15(a) and 15(b) show $\text{Imm}_{\perp}^{(\pm 105)}(x, y, z = 39 \text{ nm}, \omega)$

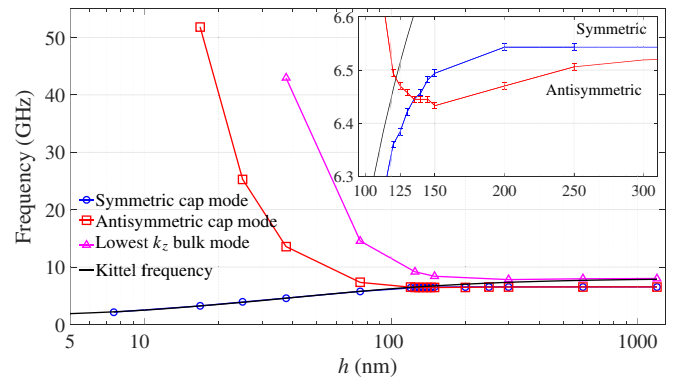


FIG. 19. Dependence of frequency on h for the lowest- k_z (000) bulk mode, symmetric (00g) cap mode, and antisymmetric (00u) cap mode of a YIG cylinder with $d = 75$ nm. Also shown is the frequency predicted by the Kittel expression. The inset shows the region where the symmetric cap mode crosses over the antisymmetric cap mode for small h . In the region below about 100 nm, the (00g) mode replaces the (000) mode as the quasi-uniform mode we associate with the Kittel formula.

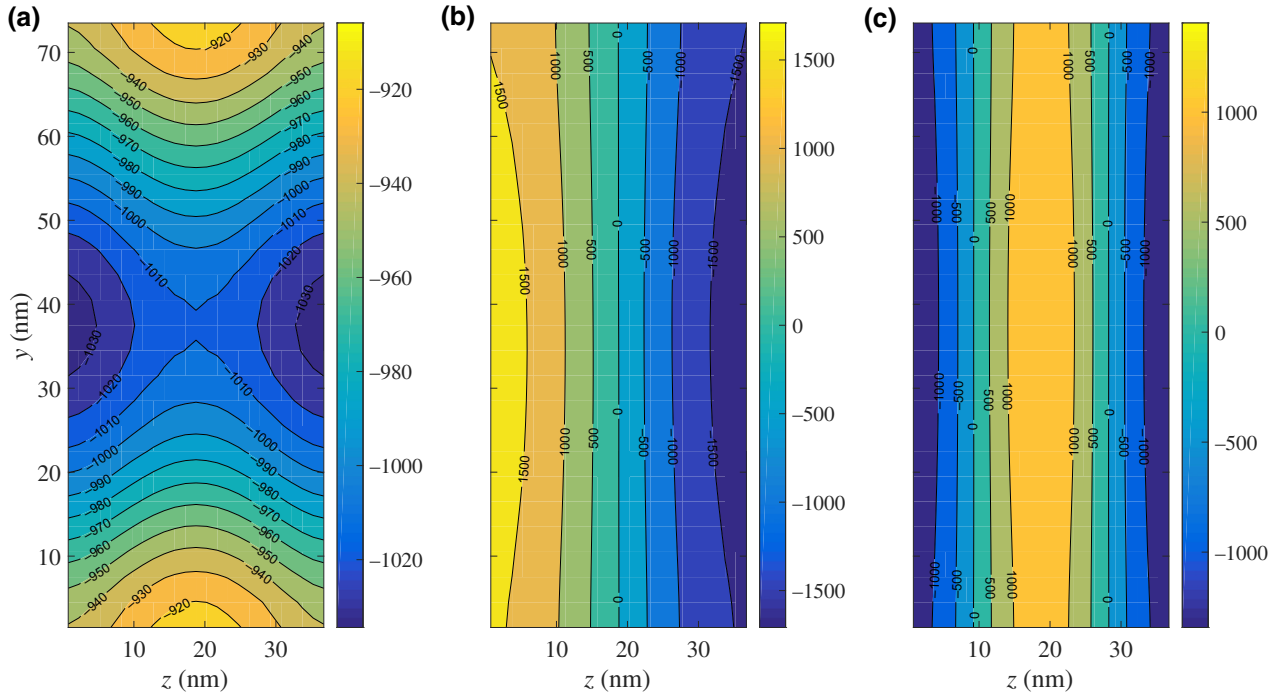


FIG. 20. Contours of constant intensity for three modes of a YIG cylinder with $d = 75$ nm and $h = 37.5$ nm. (a) 4.59-GHz symmetric (00g) cap mode, corresponding to the Kittel mode in the thin-disk limit; notably, it has no nodes. (b) 13.57-GHz antisymmetric (00u) cap mode. (c) 42.97-GHz (000) bulk mode.

and $\text{Rem}_{\perp}^{(\pm 105)}(x, y, z = 39 \text{ nm}, \omega)$, while Fig. 15(c) shows $\text{Rem}_{\perp}^{(\pm 105)}(x = 0, y, z, \omega)$. (We recall that $z = 39$ nm is the midplane of the seventh layer of cells from the bottom of the cylinder.) Notably, the mode patterns in the x - y plane now display nodes since the modes with $p = +1$ and $p = -1$ interfere to form a partial standing wave. Our plot in the y - z plane contains the two end nodes, arising from orthogonality to the cap modes discussed above (the patterns for which we do not show), as well as the five interior nodes. If we use the projection technique described in Appendix B, we can again separate the two modes. This is shown in Figs. 16(a) and 16(b), where we plot $\text{Rem}_{\perp}^{(+105)}(x, y, z = 39 \text{ nm}, \omega)$ and $\text{Rem}_{\perp}^{(-105)}(x, y, z = 39 \text{ nm}, \omega)$. These are also the modes for which we resolve the splitting via the beat pattern in Fig. 6(a).

As an example of a mode with a larger azimuthal-mode number and mixed- p character, Fig. 17 shows a plot of $\text{Rem}_{\perp}^{(\pm 305)}(x, y, z = 39 \text{ nm}, \omega)$, which has a frequency of 31.25 GHz.

Finally, we present a mode with additional radial nodes. Such a mode will have a high frequency, considering the relatively small diameter of our sample. Figures 18(a) and 18(b) show $\text{Rem}_{\perp}^{(020)}(x, y, z = h/2, \omega)$ and $\text{Rem}_x^{(020)}(x = 0, y, z, \omega)$ for the (020) mode with a frequency of $f = 56.64$ GHz.

VII. EVOLUTION OF THE LOW-LYING MODE BEHAVIOR WITH CYLINDER HEIGHT

Although the majority of our simulations for mode patterns are carried out for a YIG cylinder with $d = 2a = 75$ nm and $h = 300$ nm, the behavior of the three lowest-lying $p = 0$ modes, (000), (00g), and (00u), is studied over a much-wider range of h , extending from 7.5 to 1200 nm [40]. Figure 19 shows the frequencies emerging from the OOMMF simulations together with the predictions based on the Kittel expression, Eq. (2), according to the demagnetization coefficients found by Joseph and Schlomann [41]. Importantly, we see that the (00g) cap mode evolves into the dominant mode in the thin-disk limit, while the (000) bulk mode becomes dominant (although lying slightly higher in frequency) in the long-cylinder limit. The Kittel formula, which is a single equation, actually describes two different modes in these limits and does not apply well to any mode for $150 \text{ nm} \lesssim h \lesssim 300 \text{ nm}$. The level crossing of the (00g) and (00u) modes does not violate the Wigner-von Neumann anticrossing theorem due to their even and odd character. Furthermore, the apparent violation of the ordering of energy levels of one-dimensional (1D) Schrodinger equations is resolved by noting that the dipole-dipole interaction is a *nonlocal* perturbation, which puts the eigenvalue problem outside the Sturm-Liouville class.

It is clear from this discussion that the true behavior of the dominant FMR response cannot be described by a simple Kittel-like expression; a characterization in terms of demagnetization coefficients is inadequate and glosses over the spatial complexity of the mode with the greatest spectral weight in a uniformly excited sample.

Some mode patterns for a YIG cylinder with $d = 75$ nm and $h = 37.5$ nm are shown in Fig. 20. The cell size for these simulations is $3 \times 3 \times 1.5$ nm³. Figure 20(a) shows the 4.59-GHz symmetric (00g) cap mode, which, for these dimensions, has become the dominant mode. It is a cap mode in name only, since it spans the entire sample. Rather than the planar constant-amplitude contours encountered in the longer cylinders, this mode now has approximately cylindrical ones. Figure 20(b) shows the antisymmetric cap mode for a cylinder with the same dimensions, which now has a significantly higher frequency of 13.57 GHz; here, the contours of constant amplitude run approximately parallel to the faces, indicating that the odd mode has substantially changed character from the even one. Lastly, we show the bulk mode in Fig. 20(c). Consistent with the results in Fig. 19, this mode has the highest frequency, 42.97 GHz. The contours of constant amplitude run approximately parallel to the faces, and we obtain a quite regular sine wave, with one complete wavelength along z .

VIII. CONCLUSIONS AND POSSIBLE APPLICATIONS

We have explored the mode structure of nanoscopic cylinders of yttrium iron garnet, both analytically and through many-spin simulations, in a regime where the effects of exchange dominate the response. In addition to the extended (bulk) modes, which can be classified in terms of the azimuthal, radial, and axial mode numbers, designated as p , n_r , n_z , we find symmetric and antisymmetric combinations of cap modes that are localized at each of the cylinder faces. In all cases, they lie lower in frequency than the accompanying family of modes n_z for given azimuthal and radial mode numbers p and n_r . When examining the height dependence, we find that the dominant FMR response *cannot* be precisely described by a simple Kittel-like formula. How this picture would change in passing to the dipole-dominated limit is deserving of additional study.

By way of applications, there is a growing effort directed at using magnetic bits for computation as well as data storage. In particular, it has been demonstrated that the required logic operations can be accomplished with lines and arrays of dipole-coupled single-domain bar magnets with dimensions of a few hundred nanometers [42]. While promising, this approach is still restricted to what can be done using binary macrospin flips (and cascades thereof) of the individual magnets.

Looking further ahead, it is natural to ask if logic functions can be performed by exploiting the *internal* dynamics of nanoparticles. For the case of waveguide-based operations, this is already a worldwide activity [43]. But here we envision exciting (and mixing) large-amplitude resonant modes within a single nanoparticle. This can involve a single or multiple inputs applied simultaneously or sequentially, with different microwave frequencies and/or polarizations. When the particles are small, the various modes are well separated and can be addressed individually and rapidly. By exploiting intrinsic nonlinearities and optimizing the sample dimensions (to tune the mode frequencies), different pump frequencies can be efficiently mixed, a topic we are exploring independently. Progress in this direction requires an understanding of the low-amplitude mode structure of the particles involved.

Apart from the cap modes, the modes studied here are all extended in character and in that sense are the standing-wave counterpart of the plane-wave modes that are the typical starting point of most nonlinear analyses. However, ongoing simulations of nanoscale cylinders and elliptical disks at large precession amplitudes display instabilities involving the edge nucleation of dynamic vortex and antivortex modes. Possibly related instabilities occur at domain walls in stripes [44,45]. The connection between such states and low-lying extended modes in understanding large-amplitude precession dynamics in nanomagnets is currently unclear.

ACKNOWLEDGMENTS

This research is carried out under the support of the U.S. Department of Energy through Grant No. DE-SC0014424. This research is supported, in part, through the computational resources and staff contributions provided by the Quest High-Performance Computing Facility at Northwestern University, which is jointly supported by the Office of the Provost, the Office for Research, and Northwestern University Information Technology.

APPENDIX A: THE HERRING-KITTEL EQUATION

The HK expression, given earlier as Eq. (3), is

$$\omega^2 = \gamma^2 (H_{\text{in},z} + D_{\text{ex}} k^2) (H_{\text{in},z} + 4\pi M_0 \sin^2 \theta + D_{\text{ex}} k^2), \quad (\text{A1})$$

where we write $H_{\text{in},z} \equiv H_0 - 4\pi N_{\parallel} M_0$, with N_{\parallel} as an axial demagnetization coefficient, and

$$D_{\text{ex}} = \frac{2A_{\text{ex}}}{M_0}, \quad (\text{A2})$$

which fixes the exchange-energy density used in the OOMMF simulation,

$$E_{\text{ex}} = \frac{A_{\text{ex}}}{M_0^2} \sum_{ij} \frac{\partial M_j}{\partial x_i} \frac{\partial M_j}{\partial x_i}. \quad (\text{A3})$$

To understand the remarkable agreement between our OOMMF results and this formula, let us recall how it is derived.

The linearized Landau-Lifshitz equation is

$$\frac{d\mathbf{m}}{dt} = \gamma \hat{\mathbf{z}} \times \left(H_{\text{in},z} \mathbf{m} - M_0 \mathbf{h} + \frac{2A_{\text{ex}}}{M_0} \nabla^2 \mathbf{m} \right), \quad (\text{A4})$$

where \mathbf{h} is the dynamic demagnetization (or dipolar) field induced by \mathbf{m} . Fourier transforming with respect to space and assuming a time dependence, $e^{-i\omega t}$, we obtain

$$-i\omega \mathbf{m}_k = \gamma \hat{\mathbf{z}} \times \left(H_{\text{in},z} \mathbf{m}_k - M_0 \mathbf{h}_k - \frac{2A_{\text{ex}}}{M_0} k^2 \mathbf{m}_k \right). \quad (\text{A5})$$

The field \mathbf{h} is governed by the Maxwell equations,

$$\nabla \cdot \mathbf{h} = -4\pi \nabla \cdot \mathbf{m}, \quad \nabla \times \mathbf{h} = 0, \quad (\text{A6})$$

together with the requirements that the normal component of $\mathbf{b} = \mathbf{h} + 4\pi \mathbf{m}$ and the tangential component of \mathbf{h} be continuous at the boundary of the particle. If we now Fourier transform Eq. (A6), and simply *ignore* the effects of the boundary conditions, we obtain

$$\mathbf{h}_k = -4\pi \frac{\mathbf{k} \cdot \mathbf{m}_k}{k^2} \mathbf{k}. \quad (\text{A7})$$

Inserting (A7) into Eq. (A5), requiring the equations for the resulting two components to be compatible, and taking $H_{\text{in},z}$ to be homogeneous, leads immediately to the HK formula, Eq. (A1).

From the above derivation, we see that, qualitatively, the HK approximation accounts for the axial (static) demagnetization but neglects some part of the transverse contribution. Since the dipole-dipole interaction is long range, this neglect is qualitatively profound and quantitatively valid only for short wavelengths, when $ka \gtrsim 1$. When this condition is satisfied, we can argue that the magnetic charges induced on the ‘‘lateral’’ surface by \mathbf{m} change sign rapidly on a length scale of k^{-1} , so the field produced by them dies off on the same length scale and may be ignored in the bulk of the particle. To further clarify this behavior, we will derive the HK formula in a second way.

As is known from magnetostatics, the (normalized) magnetic field, $\mathbf{h}(\mathbf{r})$, can be regarded as arising from a

magnetic charge density, $\nabla \cdot \mathbf{m}(\mathbf{r})$, according to

$$\mathbf{h}(\mathbf{r}) = -4\pi \int_{V^+} \frac{(\mathbf{r} - \mathbf{r}')}{|\mathbf{r} - \mathbf{r}'|^3} \nabla' \cdot \mathbf{m}(\mathbf{r}') d^3 r'. \quad (\text{A8})$$

The integral here is taken to extend infinitesimally beyond the particle volume, as indicated by the superscript in V^+ . In this way, both volume and surface charges are included. If we Fourier transform this equation, we obtain

$$\mathbf{h}_k = -4\pi \int d^3 k' \frac{\mathbf{k}' \cdot \mathbf{m}_{k'}}{k'^2} \mathbf{k}' \chi_{k-k'}, \quad (\text{A9})$$

where χ_k is the Fourier transform of unity over the particle volume:

$$\chi_k = \frac{1}{(2\pi)^3} \int_{V^+} e^{-i\mathbf{k} \cdot \mathbf{r}} d^3 r. \quad (\text{A10})$$

We can write Eq. (A9) more compactly as

$$\mathbf{h}_k = -4\pi \left(\frac{\mathbf{k} \cdot \mathbf{m}_k}{k^2} \mathbf{k} \right) * \chi_k \quad (\text{A11})$$

where $*$ denotes a convolution. For a cylinder of height h and radius a ,

$$\chi_k = \frac{\pi a^2 h \sin k_z h}{(2\pi)^3} \frac{2J_1(k_{\perp} a)}{k_{\perp} h} \frac{1}{k_{\perp} a}. \quad (\text{A12})$$

When $k_z h \gtrsim 1$ and $k_{\perp} a \gtrsim \pi$ in the convolution in Eq. (A11), χ_k can be approximated by a delta function, $\delta(\mathbf{k})$, and we recover Eq. (A7). For smaller k , this approximation is invalid.

APPENDIX B: RELATIONSHIP BETWEEN STANDING AND RUNNING WAVES IN φ

The magnetization fields corresponding to running waves associated with orbital angular momentum, p and $-p$ (with $p > 0$), have the form

$$\mathbf{m}_p(\mathbf{r}, t) = F(r, z) [\cos(p\varphi - \omega t) \hat{\mathbf{x}} - \sin(p\varphi - \omega t) \hat{\mathbf{y}}], \quad (\text{B1a})$$

$$\mathbf{m}_{-p}(\mathbf{r}, t) = F(r, z) [\cos(-p\varphi - \omega t) \hat{\mathbf{x}} - \sin(-p\varphi - \omega t) \hat{\mathbf{y}}], \quad (\text{B1b})$$

where $F(r, z)$ is an unspecified function. By superposing these fields, we obtain a standing-wave pattern,

$$\mathbf{m}_p^s(\mathbf{r}, t) = \mathbf{m}_p + \mathbf{m}_{-p} = F(r, z) \cos(p\varphi) \times [\cos(\omega t) \hat{\mathbf{x}} + \sin(\omega t) \hat{\mathbf{y}}]. \quad (\text{B2})$$

We wish to recover the running-wave patterns from a knowledge of the standing-wave pattern. To do this, we

first transform the latter by rotating the amplitude by $\pi/2p$ and the vector direction by $\pi/2$. The transformed field is

$$\begin{aligned} \mathbf{m}_p^T(\mathbf{r}, t) &= \mathbf{m}_p^s[r, z, \varphi - (\pi/2p), t + (\pi/2\omega)], \\ &= F(r, z) \sin(p\varphi)[- \sin(\omega t)\hat{\mathbf{x}} + \cos(\omega t)\hat{\mathbf{y}}]. \end{aligned} \quad (\text{B3})$$

It is now easy to see that the difference of the transformed and original stationary-wave pattern gives us \mathbf{m}_p :

$$\mathbf{m}_p(\mathbf{r}, t) = \frac{[\mathbf{m}_p^s(\mathbf{r}, t) - \mathbf{m}_p^T(\mathbf{r}, t)]}{2}. \quad (\text{B4a})$$

Likewise, the sum gives \mathbf{m}_{-p} :

$$\mathbf{m}_{-p}(\mathbf{r}, t) = \frac{[\mathbf{m}_p^s(\mathbf{r}, t) + \mathbf{m}_p^T(\mathbf{r}, t)]}{2}. \quad (\text{B4b})$$

What this means is the following. Supposing OOMMF produces a pattern that has p nodal lines in φ at some fixed time. We denote this pattern by \mathbf{m}_p^s , as above. We then consider the vector fields

$$\begin{aligned} \begin{bmatrix} m_{\pm p,x}(r, z, \varphi) \\ m_{\pm p,y}(r, z, \varphi) \end{bmatrix} &= \frac{1}{2} \begin{bmatrix} m_{p,x}^s(r, z, \varphi) \\ m_{p,y}^s(r, z, \varphi) \end{bmatrix} \\ &\mp \frac{1}{2} \begin{bmatrix} -m_{p,y}^s(r, z, \varphi - \pi/2p) \\ m_{p,x}^s(r, z, \varphi - \pi/2p) \end{bmatrix}. \end{aligned} \quad (\text{B5})$$

If these combinations are used as initial conditions in OOMMF, they should evolve into $+p$ and $-p$ running waves, as indicated. In this way, we can obtain positive confirmation that these running waves are indeed eigenmodes; this is how we separate the $+p$ and $-p$ modes shown in Figs. 15 and 16.

not gadolinium gallium garnet), achieving long mode lifetimes at low temperatures is anticipated. Nanocylinders can then be patterned and excited by superconducting antennas, wherein close coupling can be achieved together with locally tailored field profiles to more effectively couple to specific modes.

- [6] M. J. Donahue and D. G. Porter, OOMMF User's Guide, Version 1.0, NISTIR 6376, National Institute of Standards and Technology, Gaithersburg, MD (Sept 1999).
- [7] R. D. McMichael and M. D. Stiles, Magnetic normal modes of nanoelements, *J. Appld. Phys.* **97**, 10590 (2005).
- [8] A. Yamaguchi, K. Motoi, A. Hirohata, H. Miyajima, Y. Miyashita, and Y. Sanada, Broadband ferromagnetic resonance of Ni81Fe19 wires using a rectifying effect, *Phys. Rev. B* **78**, 104401 (2008).
- [9] U. Ebels, J. L. Duvail, P. E. Wigen, L. Piraux, L. D. Buda, and K. Ounadjela, Ferromagnetic resonance studies of Ni nanowire arrays, *Phys. Rev. B* **64**, 144421 (2001).
- [10] C. A. Ramos, M. Vazquez, K. Nielsch, K. Pirola, J. Rivas, R. B. Wehrspohn, M. Tovar, R. D. Sanchez, and U. Gösele, *J. Mag. Mag. Mater.* **272–276**(Part 3), 1652 (2004).
- [11] A. del Campo and C. Greiner, SU-8: A photoresist for high-aspect-ratio and 3D submicron lithography, *J. Micromech. Microeng.* **17**, R81 (2007).
- [12] L. D. Landau and E. M. Lifshitz, *Course in Theoretical Physics* (Statistical Physics Part II Pergamon Press, Oxford, 1980), Section 69.
- [13] C. Kittel, On the theory of ferromagnetic resonance absorption, *Phys. Rev.* **73**, 155 (1948).
- [14] Exciting such modes with a uniform microwave field requires they have an even number of nodes, otherwise the net interaction averages to zero. To address this problem, highly efficient antennas with multiple elements that are spaced to spatially resonate with some set of modes have recently been employed: Jinho Lim, Wonbae Bang, Jonathan Trossman, Andreas Kreise, Matthias Benjamin Jungfleisch, Axel Hoffmann, C. C. Tsai, and John B. Ketterson, Direct detection of multiple backward volume modes in yttrium iron garnet at micron scale wavelengths, *Phys. Rev. B* **99**, 014435 (2019).
- [15] F. Bloch, On the theory of ferromagnetism, *Z. Physik* **61**, 206 (1930). On the Theory of the Exchange Problem and the Appearance of Retentive Ferromagnetic, *Z. Physik* **74**, 295 (1932).
- [16] A. M. Clogston, H. Suhl, L. R. Walker, and P. W. Anderson, Possible source of line width in ferromagnetic resonance, *Phys. Rev.* **101**, 903 (1956).
- [17] A. M. Clogston, H. Suhl, L. R. Walker, and P. W. Anderson, Ferromagnetic line width in insulating materials, *J. Phys. Chem. Solids* **1**, 129 (1956).
- [18] J. E. Mercereau and R. P. Feynman, Physical conditions for ferromagnetic resonance, *Phys. Rev.* **104**, 63 (1956).
- [19] L. R. Walker, Magnetostatic modes in ferromagnetic resonance, *Phys. Rev.* **105**, 390 (1957).
- [20] R. I. Joseph and E. Schlomann, Theory of magnetostatic modes in long, axially magnetized cylinders, *J. Appl. Phys.* **32**, 1001 (1961).
- [21] R. Arias and D. L. Mills, Theory of spin excitations and the microwave response of cylindrical ferromagnetic nanowires, *Phys. Rev. B* **63**, 134439 (2001).

- [1] Christophe Thirion, Wolfgang Wernsdorfer, and Dominique Mailly, Switching of magnetization by nonlinear resonance studied in single nanoparticles, *Nat. Mater.* **2**, 524 (2003).
- [2] H. Sato, T. Kano, T. Nagasawa, K. Mizushima, and R. Sato, Magnetization Switching of a Co/Pt Multilayered Perpendicular Nanomagnet Assisted by a Microwave Field with Time Varying Frequency, *Phys. Rev. Appl.* **9**, 054011 (2018).
- [3] Y. Li, V. V. Naletov, O. Klein, J. L. Prieto, M. Muñoz, V. Cros, P. Bortolotti, A. Anane, C. Serpico, and G. de Loubens, Nutation Spectroscopy of a Nanomagnet Driven into Deeply Nonlinear Ferromagnetic Resonance, *Phys. Rev. X* **9**, 041036 (2019).
- [4] For a recent example of zero-field resonances in a nano-scale object see: Wonbae Bang, F. Montoncello, M. T. Kaffash, A. Hoffmann, J. B. Ketterson, and M. B. Jungfleisch, Ferromagnetic resonance spectra of permalloy nano-ellipses as building blocks for complex magnonic lattices, *J. Appl. Phys.* **126**, 203902 (2019).
- [5] If technical issues associated with growing high-quality YIG films on nonmagnetic substrates can be solved (i.e.,

- [22] C. Herring and C. Kittel, On the theory of spin waves in ferromagnetic media, *Phys. Rev.* **81**, 869 (1951).
- [23] G. Venkat, D. Kumar, M. Franchin, O. Dmytriiev, M. Mruczkiewicz, H. Fangohr, A. Barman, M. Krawczyk, and A. Prabhakar, Proposal for a standard micromagnetic problem: Spin wave dispersion in a magnonic waveguide, *IEEE Trans. Magn.* **49**, 524 (2013).
- [24] L. D. Landau and E. M. Lifshitz, *Statistical Physics Part II*, Pergamon Press, Section 69; the form written here follows Herring and Kittel.
- [25] This argument is standard and can be found in many books. See, e.g., R. Shankar, *Principles of Quantum Mechanics*, Plenum, New York, 1980, Exercise 12.5.1 and Fig. 12.1.
- [26] See, e.g., Anupam Garg, *Classical Electromagnetism in a Nutshell* (Princeton University Press, Princeton, NJ, 2012), pp. 174–177, and 239–240.
- [27] See Eqs. (19), (23), and (24) in Ref. [20].
- [28] R. W. Damon and J. R. Eshbach, Magnetostatic modes of a ferromagnet slab, *J. Phys. Chem. Solids* **19**, 308 (1961).
- [29] See the unnumbered equation two equations above Eq. (22) in Ref. [19].
- [30] H. A. Bethe and E. E. Salpeter, *Quantum Mechanics of One and Two Electron Atoms* (Springer, Berlin, 1957), Sections 29 and 30.
- [31] W. S. Ament and G. T. Rado, Electromagnetic effects of spin wave resonance in ferro-magnetic metals, *Phys. Rev.* **97**, 1558 (1955).
- [32] Amikam Aharoni, *Introduction to the Theory of Ferromagnetism* (Oxford, 1996), p. 178.
- [33] See, e.g., C. M. Bender and S. Orszag, *Advanced Mathematical Methods for Scientists and Engineers* (McGraw-Hill, 1978), Chapter 9.
- [34] This has the virtue of replacing the discrete OOMMF field profile with a continuous one; it also gives somewhat better agreement with the simulated OOMMF mode profiles.
- [35] M. Sato and Y. Ishii, Simple and approximate expressions of demagnetizing factors of uniformly magnetized rectangular rod and cylinder, *J. Appl. Phys.* **66**, 983 (1989).
- [36] A. G. Gurevich and G. A. Melkov, *Magnetization Oscillations and Waves* (CRC Press, Boca Raton, 1996).
- [37] It can also drive additional modes with some overlap on the chosen mode at some initial instant in time.
- [38] Alternatively, we can Fourier transform the simulated form of $\bar{m}_r(z, r, \omega)$ along z , where the bar indicates a radial average, and identify the peak in the spectrum. Since our description is only semiquantitative, this procedure is not attempted.
- [39] In particular, Eq. (A11) cannot be replaced by Eq. (A7) in Appendix A. In this regard, we find the discussion by L. R. Walker, Resonant Modes of Ferromagnetic Spheroids, *J. Appl. Phys.* **29**, 318-324 (1958), and his Fig. 6 to be particularly germane.
- [40] The simulations are done with cell dimensions of $3 \times 3 \text{ nm}^2$ in the x and y directions, and the dimension Δz along the z direction is adjusted to give varying numbers of layers, depending on the height, h . The number of layers varies from 10 for $h = 7.5 \text{ nm}$, to 25 for $h = 16.8$ to 145 nm , and either 25 or 50 for $h \geq 150 \text{ nm}$. The choice of 25 layers is enough to capture the spatial variation of the three modes we are seeking in this section. It is more important to increase the run time (by as much as a factor of 8) to resolve the modes in frequency.
- [41] R. I. Joseph and E. Schlomann, Demagnetizing field in non-ellipsoidal bodies, *J. Appl. Phys.* **36**, 1579 (1965).
- [42] For a review see: M. T. Niemier, G. H. Bernstein, G. Csaba, A. Dingler, X. S. Hu, S. Kurtz, S. Liu, J. Nahas, W. Porod, M. Siddiq, and E. Varga, Nanomagnet logic: Progress toward system-level integration, *J. Phys. Condens. Matter* **23**, 493202 (2011).
- [43] Abdulqader Mahmoud, Florin Ciubotaru, Frederic Vanderveken, Andrii V. Chumak, Said Hamdioui, Christoph Adelman, and Sorin Cotozana, Introduction to spin wave computing, *J. Appl. Phys.* **128**, 161101 (2020).
- [44] D. J. Clarke, O. A. Tretiakov, G.-W. Chern, Ya. B. Bazaliy, and O. Tchernyshyov, Dynamics of a vortex domain wall in a magnetic nanostrip: Application of the collective-coordinate approach, *Phys. Rev. B* **78**, 134412 (2008).
- [45] M. Klaui, Topical review: Head-to-head domain walls in magnetic nanostructures, *J. Phys. Condens. Matter* **20**, 313001 (2008).